Electronic Transport Phenomena in Low Dimensional and Topological Materials

Songci Li

A dissertation
submitted in partial fulfillment of the
requirements for the degree of

Doctor of Philosophy

University of Washington

2017

Reading Committee:

Anton Andreev, Chair

Boris Spivak

David Cobden

Program Authorized to Offer Degree:
Physics

University of Washington

Abstract

Electronic Transport Phenomena in Low Dimensional and Topological Materials

Songci Li

Chair of the Supervisory Committee:
Professor Anton Andreev
Department of Physics

This dissertation focuses on electron transport properties in topologically nontrivial conductors (chiral *p*-wave superconductor Sr_2RuO_4 and stackings of van der Waals solids(vdWs)) and topological material, Weyl semimetals. Chiral *p*-wave superconductors exhibit spontaneous time reversal symmetry breaking due to the unconventional pairing order parameter. Violation of time reversal symmetry should manifest itself in anomalous transport effects analogous to anomalous Hall effect in ferromagnetic metals. We develop a semiclassical transport theory of several such effects: anomalous Hall effect, anomalous thermal Hall conductivity and polar Kerr effect for microwave radiation. The photogalvanic effects are studied in the van der Waals solids. Our findings predict a novel mechanism generating polarization dependent photocurrent in polar stacking of vdWs. This mechanism is attributed to the presence of a permanent electric dipole moment in the polar stacks. The recently discovered class of topological conductors, Weyl semimetals, is known for its novel surface electronic states and negative magnetoresistance (MR) due to chiral anomaly. We demonstrate that the interplay of band bending effects near the surface of the crystal and topological properties of Weyl points lead to spiral structure of energy dispersions for surface states. We also show that the interplay of chiral anomaly and Klein tunneling yields linear and negative MR of a WSM *p*-*n* junction, in contrast to positive MR in a conventional semiconductor *p*-*n* junction.

TABLE OF CONTENTS

LIST OF FIGURES

ACKNOWLEDGMENTS

I would like to express my deepest gratitude and sincere appreciation to my advisor, Prof. Anton Andreev, for his continued support and guidance throughout my graduate study. I have benefited a lot from his insight in frontiers of physics and precise understanding of the subject. Discussing physics with him has always been a pleasure to me. I am grateful to Prof. David Cobden and Prof. Boris Spivak for kindly agreeing to read the thesis. I want to thank Prof. Boris Spivak and Prof. Yuli Lyanda-Geller for the collaboration. Their comments and suggestions are an integrable part of this work. I am indebted to all my friends and colleagues in the University of Washington who have made my graduate life enjoyable. Financial support from the department of physics, University of Washington, Seattle and Department of Energy grant No. DE-FG02-07ER46452 is also acknowledged.

Chapter 1

INTRODUCTION

The electrons in solids are described in terms of Bloch waves whose wavefunctions are of the form $\psi_{\mathbf{p}}(\mathbf{r}) = e^{i\mathbf{p}\cdot\mathbf{r}/\hbar}u_{\mathbf{p}}(\mathbf{r})$, where $\mathbf{p} = \hbar\mathbf{k}$ is the quasimomentum of the electron and $u_{\mathbf{p}}(\mathbf{r})$ is the periodic part of the wavefunction. In order to study the electron transport phenomena in solid state physics two basic ingredients are needed [1, 2]: the semiclassical dynamics of electrons and the Boltzmann kinetic equation. The former treats Bloch electrons as classical particles and provides the equations of motion, in the presence of weak and slowly varying external electric field $\mathbf{E}$ and magnetic field $\mathbf{B}$,

$$\dot{\mathbf{r}} = \frac{1}{\hbar}\frac{\partial\epsilon(\mathbf{k})}{\partial\mathbf{k}}, \tag{1.1a}$$

$$\hbar\dot{\mathbf{k}} = -e\mathbf{E} - \frac{e}{c}\dot{\mathbf{r}}\times\mathbf{B}, \tag{1.1b}$$

where $\mathbf{r}$ is the coordinate, $\mathbf{k}$ is the wave vector and the electron band energy $\epsilon(\mathbf{k})$ alone determines the electron motion. The second ingredient, the Boltzmann equation, describes the evolution of a nonequilibrium electron distribution function $f(\mathbf{r},\mathbf{k})$ in the phase space $\mathbf{r}$ and $\mathbf{k}$,

$$\frac{\partial f}{\partial t} + \dot{\mathbf{r}}\cdot\frac{\partial f}{\partial\mathbf{r}} + \dot{\mathbf{k}}\cdot\frac{\partial f}{\partial\mathbf{k}} = I(f), \tag{1.2}$$

where $I(f)$ is the collision integral that depends on particular scattering processes (electron-electron scattering, electron-phonon scattering, electron-impurity scattering, etc.). Such semiclassical approach has been widely used and highly successful in explaining the electric and thermal conductivity in metals. Despite its great success, the above semiclassical approach is not complete in the description of electron transport in the modern perspective. As we shall show below, the equations of motion are augmented by a term, usually known as Berry phase tern whose origin is purely quantum mechanical.

1.1 Berry phase and modified semiclassical equations of motion

Let us begin by introducing the concept of Berry phase, which arises due to the adiabatic evolution of a quantum state. The derivation is based on Ref. [3], where the interested readers shall find more details regarding the Berry phase. Consider a quantum system described by a Hamiltonian $H(\mathbf{R}(t))$, in which $\mathbf{R}(t)$ is a set of time-dependent parameters varying slowly along a path $\mathcal{C}$ in the parameter space. The instantaneous n-th energy eigenstate [1] $|n(\mathbf{R})\rangle$ of $H(\mathbf{R})$ is found by

$$H(\mathbf{R})|n(\mathbf{R})\rangle = \epsilon_n(\mathbf{R})|n(\mathbf{R})\rangle, \tag{1.3}$$

up to an overall phase factor. Adiabatic evolution, or more precisely quantum adiabatic theorem dictates that if the system is initially prepared in its n-th energy eigenstate, the system will remain in the n-th instantaneous eigenstate in the course of evolution. Such reasoning enables us to find the quantum state at time t in the following form,

$$|\psi_n(t)\rangle = \exp\left[-\frac{i}{\hbar}\int_0^t \epsilon_n(\mathbf{R}(t')dt'\right] \exp\left(i\gamma_n(t)\right)|n(\mathbf{R}(t))\rangle, \tag{1.4}$$

where the first exponential factor is the usual dynamical phase factor, while an additional phase factor has form of a path integral along $\mathcal{C}$ in the parameter space,

$$\gamma_n(t) = \int_{\mathcal{C}} d\mathbf{R}\cdot\mathcal{A}_n(\mathbf{R}), \quad \mathcal{A}_n(\mathbf{R}) = i\langle n(\mathbf{R}(t))|\boldsymbol{\nabla}_{\mathbf{R}}|n(\mathbf{R}(t))\rangle. \tag{1.5}$$

$\mathcal{A}_n(\mathbf{R})$ is what is called Berry connection or Berry vector potential, which is a gauge dependent quantity, and hence γ_n. For quite a long time this led to the conclusion that one can always have a suitable gauge choice to eliminate γ_n. However, in the case of cyclic evolution of the system, where $\mathcal{C}$ forms a closed path in the parameter space, γ_n becomes gauge-invariant (it can only change by an integer multiple of 2π). Therefore for cyclic adiabatic evolution, a gauge-invariant phase, formally known as Berry phase, can be defined as follows,

$$\gamma_n = \oint_{\mathcal{C}} d\mathbf{R}\cdot\mathcal{A}_n(\mathbf{R}). \tag{1.6}$$

---

[1] we only deal with the case of nondegenerate energy eigenstates

Invoking the Stokes's theorem, we can rewrite Eq. (1.6) in a form of surface integral,

$$\gamma_n = \int_{\mathcal{S}} d\mathcal{S} \cdot \mathbf{\Omega}_n(\mathbf{R}), \quad \mathbf{\Omega}_n(\mathbf{R}) = \mathbf{\nabla}_{\mathbf{R}} \times \mathcal{A}_n(\mathbf{R}). \tag{1.7}$$

$\mathbf{\Omega}_n(\mathbf{R})$ is called the Berry curvature. It is gauge invariant and can be intuitively interpreted as the magnetic field in the parameter space.

Having introduced the basic concept of Berry phase and Berry curvature in a generic system with time-dependent parameters, we shift our focus to its application in solid state physics. The band theory of crystal solids centers on a $\mathbf{k}$-dependent Hamiltonian (Bloch Hamiltonian) and energy eigenstate, which is just the periodic part of the Bloch wavefunction, $u_{n\mathbf{k}}(\mathbf{r})$. We can thus identify wave vector $\mathbf{k}$ as the parameter and the Brillouin zone as the parameter space. With such identification the Berry curvature can be defined as

$$\mathbf{\Omega}(\mathbf{k}) = \mathbf{\nabla}_{\mathbf{k}} \times \langle u_n(\mathbf{k}) | i\mathbf{\nabla}_{\mathbf{k}} | u_n(\mathbf{k}) \rangle, \tag{1.8}$$

depending only on the wavefunction of the Bloch electron. We are now in a position to present the modified equations of motion of Bloch electrons in a static electromagnetic field,

$$\dot{\mathbf{r}} = \frac{1}{\hbar}\frac{\partial \varepsilon_n(\mathbf{k})}{\partial \mathbf{k}} - \dot{\mathbf{k}} \times \mathbf{\Omega}_n(\mathbf{k}), \tag{1.9a}$$

$$\hbar\dot{\mathbf{k}} = -e\mathbf{E} - \frac{e}{c}\dot{\mathbf{r}} \times \mathbf{B}, \tag{1.9b}$$

The derivation of Eq. (1.9) relies on the construction of a wave packet from the Bloch state and the details of which can be found in Refs. [4] and [5]. We would like to point out that Eq. (1.9) differs from Eq. (1.1) in two aspects. First, the electron velocity acquires a correction $\dot{\mathbf{k}} \times \mathbf{\Omega}_n(\mathbf{k})$ due to the Berry curvature. Second, the electron band energy also changes to $\varepsilon_n(\mathbf{k}) = \epsilon_n(\mathbf{k}) - \mathbf{m}_n(\mathbf{k}) \cdot \mathbf{B}$, where

$$\mathbf{m}_n(\mathbf{k}) = -i\frac{e}{2\hbar}\langle \mathbf{\nabla}_{\mathbf{k}} u_n(\mathbf{k}) | \times \left[H(\mathbf{k}) - \epsilon_n(\mathbf{k})\right] | \mathbf{\nabla}_{\mathbf{k}} u_n(\mathbf{k}) \rangle, \tag{1.10}$$

can be seen as the magnetic moment due to self-rotation of the electron wavepacket.

It is worth mentioning the symmetry properties of the Berry curvature under time reversal and spatial inversion. It is not difficult to see that if the system has time reversal symmetry,

$$\boldsymbol{\Omega}_n(\mathbf{k}) = -\boldsymbol{\Omega}_n(-\mathbf{k}),\ \boldsymbol{m}_n(\mathbf{k}) = -\boldsymbol{m}_n(-\mathbf{k}).$$

If the system possesses spatial inversion symmetry,

$$\boldsymbol{\Omega}_n(\mathbf{k}) = \boldsymbol{\Omega}_n(-\mathbf{k}),\ \boldsymbol{m}_n(\mathbf{k}) = \boldsymbol{m}_n(-\mathbf{k}).$$

The above symmetry analysis implies that $\boldsymbol{\Omega}_n(\mathbf{k})$ and $\boldsymbol{m}_n(\mathbf{k})$ vanish identically in the momentum space if the crystal solid has both time reversal and spatial inversion symmetry. As a consequence, the equations of motion reduce to the form of Eq. (1.1). Nevertheless, there are materials that lack either spatial inversion symmetry (e.g. graphene-Boron Nitride heterostructure) or time reversal symmetry (e.g. ferromagnetic metals), and thus the Berry curvature related terms are essential for a proper description of their transport properties. We want to conclude this section by providing an application of the Berry curvature in the anomalous Hall effect (AHE), the generation of a spontaneous Hall current without an external magnetic field. The interested readers can find more applications of Berry curvature on transport in Refs. [3] and [6].

In the present case the electron velocity receives a correction

$$-\dot{\mathbf{k}} \times \boldsymbol{\Omega}_n(\mathbf{k}) = \frac{e}{\hbar}\mathbf{E} \times \boldsymbol{\Omega}_n(\mathbf{k}).$$

As a result the Hall current can be computed as

$$\mathbf{j} = -\frac{e^2}{\hbar}\mathbf{E} \times \sum_n \int \frac{d^3\mathbf{k}}{(2\pi)^3} f_n^{(0)}(\mathbf{k})\boldsymbol{\Omega}_n(\mathbf{k}), \tag{1.11}$$

where the summation is taken over all occupied bands [2] and $f_n^{(0)}(\mathbf{k})$ is the equilibrium distribution function $f_n^{(0)}(\mathbf{k}) = 1/\left[e^{(\epsilon_n(\mathbf{k})-\mu)/k_BT} + 1\right]$. Hence the anomalous Hall conductivity can

---

[2] This is not in contradiction with the fact that the transport properties are determined by quasiparticles near the Fermi sea. It was proved by Haldane [7] that the anomalous Hall conductivity can be written as the Berry phase along a closed path on the Fermi surface

be obtained. The Berry curvature contribution to the anomalous Hall conductivity provides the modern view on Karplus and Luttinger's theory [8] on AHE and explains the anomalous velocity in their theory. As we can see this contribution depends only on the electron band structure and not on scattering off disorder in the system, it is thus dubbed as the intrinsic contribution to the AHE.

1.2 Extrinsic contributions to the AHE: skew scattering and side jump

In this section we briefly [3] review the contributions to the AHE attributable to scattering off impurities in the sample. The purpose is two fold: i) we would like to provide a complete understanding of the AHE in combination with the ending of Sec. 1.1 as we shall immediately encounter such effects in Chapter 1; ii) skew scattering and side jump effects are also pertinent to the photogalvanic effect (PGE) to be studied in Chapter 2 due to the same physical mechanism.

Historically [10, 11] skew scattering can be understood as an asymmetric scattering process that produces a scattering probability from momentum $\mathbf{k}$ to $\mathbf{k}'$, $W_{\mathbf{k}\mathbf{k}'} \propto \mathbf{k} \times \mathbf{k}' \cdot \mathbf{M}$, where $\mathbf{M}$ is the magnetization of the sample. Applying this in the Boltzmann kinetic equation results in a current perpendicular to both the longitudinal current driven by an external electric field and $\mathbf{M}$. Hence the Hall current or Hall conductivity is proportional to the transport lifetime τ. The side jump effect in the AHE, first pointed out by Berger [12], is attributed to the fact that the center of mass of a wave packet with incident wave vector $\mathbf{k}$ undergoes a sideways displacement transverse to $\mathbf{k}$ when it is scattered by a central potential. Such effect produces a Hall conductivity independent of τ. Side jump was also studied independently in Ref. [13] in the context of the PGE. As both the intrinsic and side jump contribution are independent of τ, one may raise the question how the two contributions can be distinguished. This issue has been addressed in a recent review by Sinitsyn [14]. The approach is summarized as follows.

---

[3] The interested readers can find in Ref. [9] for a thorough exposition of the AHE.

The scattering rate, $\omega_{ll'}$, is computed from the scattering T-matrix,

$$\omega_{ll'} = 2\pi |T_{ll'}|^2 \delta(\epsilon_l - \epsilon_{l'}), \tag{1.12}$$

with the index l being a combined index of both band n and momentum $\mathbf{k}$. The T-matrix element can be expressed in the Born series for a weak disorder potential V,

$$T_{ll'} \approx V_{ll'} + \sum_{l''} \frac{V_{ll''} V_{l''l'}}{\epsilon_{l'} - \epsilon_{l''} + i0^+} + \cdots . \tag{1.13}$$

Using Eqs (1.12) and (1.13) we arrive at an antisymmetric scattering rate (skew scattering rate),

$$\omega_{ll'}^{(3a)} = -(2\pi)^2 \sum_{l''} \delta(\epsilon_l - \epsilon_{l''}) \Im \langle V_{ll'} V_{l'l''} V_{l''l} \rangle_{dis} \delta(\epsilon_l - \epsilon_{l'}), \tag{1.14}$$

starting at the third order of V. There is also an antisymmetric scattering rate, $\omega_{ll'}^{(4a)}$, in the next order (proportional to V^4), which, in general, should not be excluded due to its distinct parametric dependence from $\omega_{ll'}^{(3a)}$. The side jump or the coordinate shift can be obtained by formulating an effective Lagrangian of a wave packet scattering upon a weak disorder potential. The expression is in the following gauge-invariant form,

$$\delta \mathbf{r}_{ll'} = \langle u_{l'} | i\partial_{\mathbf{k}'} u_{l'} \rangle - \langle u_l | i\partial_{\mathbf{k}} u_l \rangle - \hat{\mathbf{D}}_{\mathbf{k}',\mathbf{k}} \arg(T_{l'l}),\ \hat{\mathbf{D}}_{\mathbf{k}',\mathbf{k}} = \partial_{\mathbf{k}'} + \partial_{\mathbf{k}}, \tag{1.15}$$

where $\arg(\cdots)$ stands for the phase of a complex number. Taking into account Eqs. (1.12) and (1.15), the linearized Boltzmann equation can be cast in the form, with a driving electric field $\mathbf{E}$,

$$-e\mathbf{E} \cdot \frac{\partial \epsilon_l}{\partial \mathbf{k}} \frac{\partial f^{(0)}(\epsilon_l)}{\partial \epsilon_l} = \sum_{l'} \omega_{ll'} [f_l - f_{l'} - \frac{\partial f^{(0)}(\epsilon_l)}{\partial \epsilon_l} e\mathbf{E} \cdot \delta \mathbf{r}_{ll'}]. \tag{1.16}$$

By substituting the skew scattering rate, (1.14), into Eq. (1.16) we can deduce a corresponding contribution to the total distribution function. The square bracket term, accounting for the side jump, in Eq. (1.16) follows from the fact that the scattering from state l' to l is accompanied with the change in potential energy, $\Delta U_{ll'} = e\mathbf{E} \cdot \delta \mathbf{r}_{ll'}$, which leads to $\epsilon_{l'} - \epsilon_l = e\mathbf{E} \cdot \delta \mathbf{r}_{ll'}$, due to the conservation of energy. Consequently, the equilibrium distribution $f^{(0)}$ does not nullify the collision integral. Instead we have

$$f^{(0)}(\epsilon_l) - f^{(0)}(\epsilon_{l'}) \approx -\frac{\partial f^{(0)}(\epsilon_l)}{\partial \epsilon_l} e\mathbf{E} \cdot \delta \mathbf{r}_{ll'},$$

which is present in the square bracket of Eq. (1.16).

To conclude this section we have depicted a picture of the AHE, in which the Hall conductivity σ_H can be written as $\sigma_H = \sigma_H^{in} + \sigma_H^{sk} + \sigma_H^{sj}$. The intrinsic contribution σ_H^{in} is rooted in the Berry curvature introduced in Sec. 1.1. σ_H^{sk} and σ_H^{sj} represent skew scattering and side jump, respectively. σ_H^{sk} is proportional to the transport life time, τ, and appears in the third or higher order of the scattering potential (the lowest Born approximation fails). In a clean system at low temperature, in which τ is large, the skew scattering dominates over the intrinsic and side jump contribution as they are independent of τ.

1.3 Overview of the thesis

The first two chapters contain the application of generalized semiclassical kinetic equations to the study of electronic transport. In *Chapter 2* we apply such technique to analyze the transport phenomena in a quasi-two-dimensional metal, Sr_2RuO_4, believed to be a $p_x + ip_y$ superconductor. The time reversal symmetry of this material is spontaneously broken below the superconducting transition temperature, T_c, as a consequence of unconventional Cooper pairing. Violation of time reversal symmetry manifests itself in Hall-like effects analogous to anomalous Hall effect in ferromagnetic metals. Several of such effects, including anomalous Hall effect, anomalous thermal Hall conductivity and the polar Kerr effect, are examined in the semiclassical regime, in which the skew scattering dominates the transport phenomena.

In *Chapter 3* we focus on another novel low-dimensional material, transition metal dichalcogenide, a representative of van der Waals solids (vdWs). In particular we explore the linear and circular photogalvanic effect with the aid of semiclassical transport approach. Our findings show that the direction and magnitude of the photocurrent is controlled by light polarization and is determined by its helical or nonhelical components. The helicity-dependent ballistic photocurrent arises due to asymmetric photogeneration. The non-helical photocurrent has a ballistic contribution (dominant in sufficiently clean samples) caused by asymmetric scattering of photoexcited carriers, and a side-jump contribution. We also investigate magneto-induced photocurrent. It arises due to the Lorentz force or due to intrinsic magnetic moment related to Berry curvature.

In *Chapters 4 and 5* we study electron physics in the recently discovered three-dimensional topological material, Weyl semimetal. The band structure of such material consists of band touching points (called Weyl points or Weyl nodes) with linear dispersion relations. These band touching points are topologically protected as they can be viewed as monopoles and anti monopoles in the Brillouin zone. In *Chapter 4* we study its peculiar surface electron states whose Fermi surfaces form arcs (called Fermi arcs) connecting projections of the Weyl points onto the surface plane. In the meantime band bending near the boundary of the crystal also produces surface states. Our result show that the interplay of band bending near the crystal surface and topological properties of Weyl points gives rise to spiral structure of energy dispersions for surface states .

In *Chapter 5* the magnetotransport in Weyl semimetal is examined. Electron transport is mediated by Klein tunneling between n- and p- regions due to the relativistic nature of the particle. The chiral anomaly in Weyl semimetals plays a crucial role in the magnetoconductance of the junction. When the magnetic field orientation with the normal of the junction plane (tilting angle) is small, magnetoconductance is positive and linear in B at both weak and strong magnetic fields. In contrast, magnetoconductance in conventional p-n junctions is always negative. At large tilting angles the magnetocondutance displays non-monotonic behavior.

Finally, the content of this dissertation is based on the following publications:

- Anomalous Transport Phenomena in $p_x + ip_y$ Superconductors, S. Li, A. V. Andreev and B. Z. Spivak, Phys. Rev. B **92**, 100506(R) (2015).

- Polarization-dependent Photocurrents in Polar Stacks of van der Waals Solids, Y. B. Lyanda-Geller, S. Li and A. V. Andreev, Phys. Rev. B **92**, 241406(R) (2015).

- Spiraling Fermi Arcs in Weyl Materials, S. Li and A. V. Andreev, Phys. Rev. B **92**, 201107(R) (2015).
- Klein Tunneling and Magnetoresistance of *p*-*n* Junctions in Weyl Semimetals, S. Li, A. V. Andreev and B. Z. Spivak, Phys. Rev. B **94**, 081408(R) (2015).

Chapter 2

ANOMALOUS TRANSPORT PHENOMENA IN CHIRAL P-WAVE SUPERCONDUCTORS

Spontaneous breaking of time-reversal symmetry in superconductors with the $p_x + ip_y$ *symmetry of the order parameter allows for a class of effects which are analogous to the anomalous Hall effect in ferromagnets. These effects exist below the critical temperature,* $T < T_c$*. We develop a kinetic theory of such effects. In particular, we consider anomalous Hall thermal conductivity, the polar Kerr effect, the anomalous Hall effect, and the anomalous photo- and acousto-galvanic effects.* [1]

2.1 Introduction

One of the leading candidates for p-wave pairing in electronic systems is Sr_2RuO_4. Numerous experiments indicate that the superconducting state of Sr_2RuO_4 has odd parity, breaks time reversal symmetry and is spin triplet. [15, 16, 17, 18, 19, 20] The order parameter consistent with these experiments is given by the chiral p-wave state [21] which is an analog of the ^{3}He-A-phase. The Fourier transform of the real space order parameter $\Delta_{\alpha\beta}(\mathbf{r}-\mathbf{r}')$ has the form $\Delta_{\alpha\beta}(\mathbf{p}) \sim (p_x \pm ip_y)\mathbf{S}\cdot\boldsymbol{\sigma}_{\alpha\beta}$, where $\mathbf{S}$ is the spin of the Cooper pair, $\boldsymbol{\sigma}$ are the Pauli matrices, and α and β are spin indices. However, the observation of power law temperature dependence of specific heat [22] and NMR, [23] the absence of electric currents along edges, [24, 25, 26] and the absence of a split transition in the presence of an in-plane magnetic field [27] are inconsistent with the theoretically expected properties of a simple chiral superconductor. Consideration of additional experimental manifestations of spontaneous breaking of time-reversal symmetry in $p_x + ip_y$ superconductors may clarify the nature of superconducting

---

[1] The material presented in this Chapter is based on S. Li, A. V. Andreev and B. Z. Spivak, Phys. Rev. B **92**, 100506(R) (2015) , with minor alterations.

state in $\mathrm{Sr_2RuO_4}$.

Due to spontaneous breaking of time-reversal symmetry, $p_x + ip_y$ superconductors must exhibit anomalous transport phenomena in the absence of external magnetic fields, similar to those in metallic ferromagnets (see Refs. [3] and [9] for a review). In this chapter we develop a theory of several such effects in $p_x + ip_y$ superconductors: the anomalous Hall effect, polar Kerr effect for microwave radiation, anomalous Hall thermal conductivity, and anomalous photo- and acousto-galvanic effects.

It should be noted that p-wave superconductivity exists only in the clean regime, $l > \xi$, where electron transport may be described semiclassically. Generally, in the semiclassical regime there are three contributions to anomalous transport phenomena: skew scattering, side jumps, and the intrinsic contribution. The side jump contribution arises from the shift of the center of mass of electron wave packets during the scattering events, while the intrinsic contribution is related to the anomalous velocity due to Berry curvature. The magnitude of these contributions is independent of the mean free path. In contrast, the magnitude of the skew scattering contribution is proportional to the quasiparticle mean free path l. As a result, the skew scattering contribution exceeds the intrinsic and side jump contributions by a large factor $Cp_F l$, where p_F is the Fermi momentum, and C is the prefactor that depends on the impurity strength and the details of the band structure. In $p_x + ip_y$ superconductors $l > \xi$, the semiclassical parameter is sufficiently large, $p_F l > 10^3\hbar$, so that the condition $Cp_F l \gg 1$ is satisfied for most types of impurities. Therefore in this article we will take into consideration only the skew scattering contribution. We focus on anomalous transport phenomena in the vicinity of the critical temperature, where quasiparticles play a major role.

2.2 Kinetic scheme

Transport theory in conventional time reversal invariant superconductors was developed long ago (see for example reviews Refs. [28] and [29]). Below we generalize this approach to superconductors without time reversal symmetry, which exhibit anomalous transport phenomena. In the clean regime, $l \gg \xi$, and at sufficiently low frequencies, $\omega \ll |\Delta|$, where $|\Delta|$ is the modulus of the order parameter, the quasiparticle dynamics can be described by the Boltzmann kinetic equation for the quasiparticle distribution function $n_{\mathbf{p}}(\mathbf{r},t)$,

$$\frac{\partial n_{\mathbf{p}}(\mathbf{r},t)}{\partial t}+\frac{\partial\tilde{\epsilon}_{\mathbf{p}}}{\partial\mathbf{p}}\frac{\partial n_{\mathbf{p}}}{\partial\mathbf{r}}-\frac{\partial\tilde{\epsilon}_{\mathbf{p}}}{\partial\mathbf{r}}\frac{\partial n_{\mathbf{p}}}{\partial\mathbf{p}}=I_{st}, \tag{2.1}$$

where the collision integral $I_{st}=I_{st}^{(el)}+I_{st}^{\epsilon}$ in Eq. (2.1) describes both elastic and inelastic scattering, and

$$\tilde{\epsilon}_{\mathbf{p}}=\epsilon_{\mathbf{p}}+\mathbf{v}\cdot\mathbf{p}_s,\quad \epsilon_{\mathbf{p}}=\sqrt{\tilde{\xi}_{\mathbf{p}}^2+|\Delta|^2}, \tag{2.2a}$$

$$\tilde{\xi}_{\mathbf{p}}=\xi_{\mathbf{p}}+\Phi+\frac{\mathbf{p}_s^2}{2m},\quad \xi_{\mathbf{p}}=\frac{p^2}{2m}-\epsilon_F. \tag{2.2b}$$

In Eq. (2.2) m is the electron mass, while $\mathbf{p}_s$ and Φ, are given by

$$\mathbf{p}_s=\frac{\hbar}{2}\boldsymbol{\nabla}\chi-\frac{e}{c}\mathbf{A},\quad \Phi=\frac{\hbar}{2}\partial_t\chi+e\phi, \tag{2.3}$$

where χ is the order parameter phase, and ϕ and $\mathbf{A}$ are the scalar and vector potentials. From Eq. (2.3) one obtains the equation for the acceleration of the condensate,

$$\partial_t\mathbf{p}_s=e\mathbf{E}+\boldsymbol{\nabla}\Phi. \tag{2.4}$$

Equations (2.1)-(2.3) should be supplemented by the expression for the current density,

$$\mathbf{j} \;=\; \frac{eN}{m}\mathbf{p}_s+e\int d\Gamma\mathbf{v}n_{\mathbf{p}}, \tag{2.5}$$

and by the charge neutrality condition,

$$\nu\Phi=\int d\Gamma\,\frac{\tilde{\xi}_{\mathbf{p}}}{\tilde{\epsilon}_{\mathbf{p}}}\,n_{\mathbf{p}}, \tag{2.6}$$

that relates the gauge invariant scalar potential and the odd in ξ part of the quasiparticle distribution function, the self-consistency equation for the order parameter. Here ν is the density of states at the Fermi level, $d\Gamma=d^3p/(2\pi\hbar)^3$ and $\mathbf{v}=d\xi_{\mathbf{p}}/d\mathbf{p}$.

We work in linear response to external perturbations, and neglect corrections to equilibrium value of $|\Delta|$. We also assume that $\tau_\epsilon\gg\tau$, where τ_ϵ and τ are inelastic and elastic mean free time respectively. Therefore the main contribution to the aforementioned anomalous effects comes from elastic scattering, which is described by the collision integral

$$I_{st} = \int \left(W_{\mathbf{pp}'} n_{\mathbf{p}'} - W_{\mathbf{p}'\mathbf{p}} n_{\mathbf{p}}\right) \delta\left(\tilde{\epsilon}_{\mathbf{p}} - \tilde{\epsilon}_{\mathbf{p}'}\right) d\Gamma'. \tag{2.7}$$

Skew scattering of quasiparticles corresponds to the part of scattering probability $W_{\mathbf{pp}'}$ in Eq. (2.7) that is associated with breaking of time reversal symmetry, $\delta W_{\mathbf{pp}'} = W_{\mathbf{pp}'} - W_{-\mathbf{p}'-\mathbf{p}} \neq 0$. Thus, all the aforementioned effects are proportional to $\delta W_{\mathbf{pp}'}$. Skew scattering arises beyond the lowest Born approximation for the scattering amplitude. Below we consider point-like impurities. In the normal state such impurities scatter electrons only in the s-wave channel and do not cause skew scattering. Therefore in the superconducting state skew scattering of quasiparticles is entirely due to the breaking of time reversal symmetry by the $p_x + ip_y$ order parameter. The elastic scattering probability for quasiparticles with energy ϵ can be characterized by $\xi \equiv \xi_{\mathbf{p}}$, $\xi' \equiv \xi_{\mathbf{p}'} = \pm\xi$ and the azimuthal angles φ, φ', which define the direction of $\mathbf{p}$ and $\mathbf{p}'$ in the xy-plane. For simplicity, we assume cylindrical Fermi surface (with energy independent of p_z) and obtain for the scattering probability (see Appendix A)

$$W_{\mathbf{pp}'} = W_0 + W_1 \left[1 - \cos\left(\varphi - \varphi' + 2\delta_\epsilon\right)\right]. \tag{2.8}$$

Here δ_ϵ is the energy-dependent scattering phase shift. It is related to the normal state s-wave phase shift δ_n by

$$\delta_\epsilon = \arctan \frac{\delta_n \epsilon}{\sqrt{\epsilon^2 - |\Delta|^2}}. \tag{2.9}$$

We assume weak impurities, for which $\delta_n \approx \tan\delta_n \equiv -\pi\nu V_0$, is small. Here V_0 is the impurity pseudo-potential. [30] In this case W_0 and W_1 are given by

$$\begin{aligned} W_0(\xi, \xi') &= \frac{\zeta(\epsilon)}{2\nu\tau} \frac{(\xi + \xi')^2}{2\epsilon^2}, & (2.10\text{a}) \\ W_1(\xi, \xi') &= \frac{\zeta(\epsilon)}{2\nu\tau} \frac{|\Delta|^2}{\epsilon^2}. & (2.10\text{b}) \end{aligned}$$

Here $\tau^{-1} = 2\pi n_i \nu V_0^2$, with n_i being the impurity density, is the elastic scattering rate in the normal state. The coefficient $\zeta(\epsilon) = (\epsilon^2 - |\Delta|^2)/[\epsilon^2(1 + \delta_n^2) - |\Delta|^2]$ represents the enhancement factor of the quasiparticle scattering cross-section over the normal state value. The first term in Eq. (2.8), W_0 given by Eq. (2.10a) has the same structure as in s-wave superconductors. It describes scattering only within the same (particle-like, $\xi > 0$, or hole-like, $\xi < 0$) branch and does not lead to branch imbalance relaxation. The second term, W_1 in Eq. (2.8) is absent in s-wave superconductors. It leads to both skew scattering and scattering between branches of quasiparticle spectrum with different signs of ξ. The skew scattering cross-section, described by the $\sin(\varphi - \varphi') \sin 2\delta_\epsilon$ term in Eq. (2.8), is energy-dependent. It follows from Eqs. (2.8), (2.9), and (2.10b) that it changes sign when impurity potential V_0 changes from repulsive to attractive.

Below we consider linear response to several external perturbations and look for the quasiparticle distribution function in the form $n_{\mathbf{p}} = n^{(0)} + n^{(1)}_{\mathbf{p}}$, where $n^{(0)}$ is a locally equilibrium Fermi distribution, and $n^{(1)}_{\mathbf{p}}$ describes the deviation from equilibrium. Noting that the collision integral (2.7) is nullified by an arbitrary function $n^{(0)}(\tilde{\epsilon}_{\mathbf{p}})$ we write the linearized Boltzmann equation in the form

$$\mathcal{S}(\mathbf{p}) = \int d\Gamma' W_{\mathbf{p}\mathbf{p}'} (n^{(1)}_{\mathbf{p}} - n^{(1)}_{\mathbf{p}'}) \delta(\epsilon_{\mathbf{p}} - \epsilon_{\mathbf{p}'}), \tag{2.11}$$

where the source $\mathcal{S}(\mathbf{p})$ is obtained by linearizing the left hand side of Eq. (2.1) about the equilibrium, and its specific form of the depends on the type of perturbation.

2.3 Anomalous Transport Phenomena

2.3.1 Anomalous Hall thermal conductivity

We first consider the Hall component of the thermal conductivity κ_{xy} which describes the heat flux perpendicular to the direction (x-axis) of the temperature gradient. In this case the source term in Eq. (2.11) has the form,

$$\mathcal{S}(\mathbf{p}) = -\frac{\xi}{T} \, \mathbf{v} \cdot \boldsymbol{\nabla} T \, \frac{\partial n^{(0)}}{\partial \epsilon}. \tag{2.12}$$

The expression for the heat flux is

$$\mathbf{j}^Q \;\; = \;\; \int d\Gamma \, \epsilon_{\mathbf{p}} \, \frac{\partial \epsilon_{\mathbf{p}}}{\partial \mathbf{p}} \, n^{(1)}_{\mathbf{p}}. \tag{2.13}$$

Note that $\partial\epsilon_{\mathbf{p}}/\partial\mathbf{p} = \mathbf{v}\xi/\epsilon$ is the group velocity of the quasiparticles while $\mathbf{v}$ is the bare velocity as in a normal metal, $|\mathbf{v}| = v_F$. The solution of Eqs. (2.11), (2.12) has the form

$$n^{(1)}_{\mathbf{p}} = -\frac{\xi}{T} v_F \nabla T \frac{\partial n^{(0)}}{\partial\epsilon}\left[\alpha_s(\epsilon)\sin\varphi + \alpha_c(\epsilon)\cos\varphi\right].$$

The Hall component of the thermal conductivity tensor, κ_{xy}, is determined by $\alpha_s(\epsilon)$ in the above expression, which is given by $\alpha_s(\epsilon) = a(\epsilon)/[b^2(\epsilon) + a^2(\epsilon)]$, with

$$a(\epsilon) = \frac{\zeta(\epsilon)}{2\tau}\frac{|\Delta|^2}{2\epsilon|\xi|}\sin 2\delta_\epsilon, \tag{2.14a}$$

$$b(\epsilon) = \frac{|\xi|}{\epsilon\tau} + \frac{\zeta(\epsilon)}{2\tau}\frac{|\Delta|^2}{2\epsilon|\xi|}\left(\cos 2\delta_\epsilon + 2\right). \tag{2.14b}$$

For weak impurities, $|\delta_n| \ll 1$, we obtain, close to T_c

$$\kappa_{xy} = 3\kappa\left(\frac{|\Delta|}{\pi T}\right)^2 \delta_n, \tag{2.15}$$

where $\kappa = \pi^2\nu T D/3$ (with $D = v_F^2\tau/2$ being the diffusion constant) is the normal state thermal conductivity.

2.3.2 Polar Kerr effect

Next we consider a linearly polarized electromagnetic wave at normal incidence to the xy surface of $p_x + ip_y$ superconductor. The reflected wave is elliptically polarized with the major axis rotated with respect to the incident one by the polar Kerr angle [31]

$$\theta_k = \frac{(1 - n^2 + \kappa^2)\Delta\kappa + 2n\kappa\Delta n}{(1 - n^2 + \kappa^2)^2 + (2n\kappa)^2}, \tag{2.16}$$

where n and κ are, respectively, the real and imaginary part of the refraction index and

$$\Delta n + i\Delta\kappa = -\frac{4\pi}{\omega}\frac{(n - i\kappa)\sigma_{xy}}{n^2 + \kappa^2}, \tag{2.17}$$

where σ_{xy} is the complex ac conductivity.

In this case the electric field is uniform in the direction parallel to the surface of the sample, $\Phi = 0$, and the value of $\mathbf{p}_s(t)$ is determined by Eq. (2.4). The diagonal part of the conductivity is given by [28]

$$\sigma_{xx} \approx \sigma_D + \frac{iN_s(T)}{\omega}, \tag{2.18}$$

where $N_s(T)$ is the temperature dependent superfluid density and $\sigma_D = e^2\nu D$ is the Drude conductivity. In contrast to the thermal conductivity consideration, in the present case $n^{(0)} = 1/(\exp[\epsilon_{\mathbf{p}} + \mathbf{v}\cdot\mathbf{p}_s(t)]/T + 1)$ gives a nonvanishing contribution to the current response (via $N_s(T)$) because the superfluid momentum depends on the electric field. The Kerr angle θ is determined by the value of the Hall component of conductivity σ_{xy}.

To find σ_{xy} we seek the solution of Eq. (2.1) in the form $n = n^{(0)}(\epsilon_{\mathbf{p}}/T) + n_{\mathbf{p}}^{(1)}$. The source in Eq. (2.11) becomes

$$\mathcal{S}(\mathbf{p}) \;=\; -i\omega n_{\mathbf{p}}^{(1)} - e\mathbf{v}\cdot\mathbf{E}\frac{\partial n^{(0)}}{\partial\epsilon}, \tag{2.19}$$

where the external electric field $\mathbf{E}$ is along x-direction. The nonequilibrium distribution $n_{\mathbf{p}}^{(1)}$ has the form

$$n_{\mathbf{p}}^{(1)} = -eEv_F\frac{\partial n^{(0)}}{\partial\epsilon}\left[\beta_s(\epsilon)\sin\varphi + \beta_c(\epsilon)\cos\varphi\right]. \tag{2.20}$$

The Hall conductivity depends only on the function $\beta_s(\epsilon)$, which is given by $\beta_s(\epsilon) = a(\epsilon)/\{[b(\epsilon) - i\omega]^2 + a^2(\epsilon)\}$, with $a(\epsilon)$ and $b(\epsilon)$ being defined in Eq. (2.14). Substituting Eq. (2.20) into Eq. (3.2) we obtain the Hall conductivity in the weak impurity limit, $|\pi\nu V_0| \ll 1$, in the form

$$\begin{aligned}\sigma_{xy}(\omega) \;&=\; \sigma_D\frac{|\Delta|}{2T}\delta_n\int_0^\infty \frac{dx}{\cosh^2(\sqrt{x^2+1}|\Delta|/2T)}\\ &\quad\times\frac{x^2+1}{(-i\omega\tau x\sqrt{x^2+1} + x^2 + 3/4)^2}.\end{aligned} \tag{2.21}$$

where $x = |\xi|/|\Delta|$. At temperature close to T_c and at low frequencies, $\omega\tau \ll 1$, this expression yields

$$\sigma_{xy} = \frac{7\pi}{12\sqrt{3}}\,\delta_n\,\frac{|\Delta|}{T}\,\sigma_D. \tag{2.22}$$

This result was derived assuming $p_x + ip_y$ symmetry of the order parameter. In the $p_x - ip_y$ state the Hall conductivity σ_{xy} has opposite sign. It also changes sign if the impurity potential V_0 changes from repulsive, $\delta_n < 0$, to attractive, $\delta_n > 0$, in agreement with Ref. [32]. Note that our result for the low frequency Hall conductivity, Eq. (2.22), is proportional to the elastic mean free time τ and to the density of quasiparticles.

There is another contribution to σ_{xy} associated with the existence of the transverse component of the superfluid velocity $v_y \sim \dot{p}_x$, which is proportional to the condensate acceleration in the x-direction. It may not be obtained within the present formalism which is based on the Boltzmann kinetic equation for the quasiparticles. At $T \sim T_c$ this contribution is smaller than the quasiparticle contribution, Eq. (2.22). However at $T \ll T_c$ when the quasiparticle contribution becomes exponentially small in Eq. (2.21) it becomes the dominant contribution. The requirement for this contribution to exist is violation of Galilean invariance in the system. Thus it should exist in any crystalline superconductors with $p_x + ip_y$ symmetry. [33, 34] The conclusion that σ_{xy} remains finite even at $\omega \to 0$, and $T = 0$ is in agreement with the results presented in Fig. 2 of Ref. [33]. Galilean invariance can also be broken by impurities. The corresponding contribution to σ_{xy} is inversely proportional to the electron mean free time.

2.3.3 Hall effect for normal current injection

Let us now consider a normal metal/$p_x + ip_y$-superconductor junction, through which a steady current is flowing. At $T \ll |\Delta|$ this situation was considered in Ref. [35]. In this regime conversion of normal current to supercurrent is mediated by multiple Andreev reflections. Here we work near the critical temperature and consider a setup, in which the normal current is injected into the superconductor in the x-direction, as shown in the inset in Fig. 2.1. In this case the conversion of quasiparticle current to the supercurrent occurs in the superconductor. Just as in the case of s-wave superconductor, near T_c, the electric field penetrates into superconductor to a large distance $L_Q \gg l$, which is determined by the relaxation of imbalance between the populations of quasiparticles in electron-like, $\xi > 0$, and hole-like, $\xi < 0$ branches of the spectrum (see for example Ref. [28] and references therein). The new feature of normal current injection that appears in $p_x + ip_y$ superconductors is that skew scattering of quasiparticles generates nonequilibrium current perpendicular to the electric field. Another aspect is that, in contrast to s-wave superconductors, impurity scattering leads to branch imbalance relaxation even if the magnitude of the order parameter $|\Delta|$ is isotropic in the Fermi surface. Below we assume that the inelastic scattering rate is smaller than $1/\tau$ and thus impurity scattering gives the dominant contribution to branch imbalance relaxation.

In linear response we write the quasiparticle distribution function in the superconductor in the form $n^{(0)}(\epsilon_{\mathbf{p}}/T) + n_{\mathbf{p}}^{(1)}$. This yields the source term in Eq. (2.11)

$$\mathcal{S}(\mathbf{p}) = \frac{\xi}{\epsilon}\,\mathbf{v} \cdot \frac{\partial n_{\mathbf{p}}^{(1)}}{\partial \mathbf{r}}. \tag{2.23}$$

At length scales in excess of the mean free path we may employ the diffusive approximation. With the aid of Eq. (3.2) the Hall current j_y can be expressed in the form

$$j_y(x) = -4e\nu D\,\delta_n \int d\xi \frac{|\Delta|^2}{\xi^2} \partial_x \bar{n}_a(\xi, x), \tag{2.24}$$

where $\bar{n}_a(\xi, x)$ is the antisymmetric in ξ part of the distribution function averaged over the momentum directions. The latter satisfies the diffusion equation with relaxation

$$D \frac{\partial^2}{\partial x^2} \bar{n}_a(\xi, x) = \frac{1}{\tau_Q(\xi)} \bar{n}_a(\xi, x), \tag{2.25}$$

with energy dependent relaxation rate $\tau_Q^{-1}(\xi) = \tau^{-1}|\Delta|^2(\xi^2 + 2|\Delta|^2)/\xi^4$. The solution of Eq. (2.25) is

$$\bar{n}_a(\xi, x) = \bar{n}_a(\xi, 0) \exp\left[-x/L_Q(\xi)\right], \tag{2.26}$$

where $L_Q(\xi) = \sqrt{D\tau_Q(\xi)}$ is the energy-dependent branch imbalance relaxation length.

We work in the vicinity of the critical temperature T_c, where for typical thermal quasiparticles $\xi \sim T$, ($|\xi| \gg |\Delta|$), the relaxation lengths are long, $L_Q(\xi) = l|\xi|/|\Delta| \gg l$. These quasiparticles diffuse into the bulk of the superconductor and contribute to the gauge-invariant potential Φ given by Eq. (2.6). The boundary value of the nonequilibrium quasiparticle population, $\bar{n}_a(\xi, 0)$ in Eq. (2.26) is obtained by matching the solution of Eq. (2.25) with the solution of diffusion equation with energy relaxation for the electrons in the normal metal. The result depends on both the inelastic mean free path in the normal metal, l_e, and the branch imbalance relaxation length L_Q in the superconductor. For $l_e \gg L_Q$ the boundary condition is

$$\bar{n}_a(\xi,0) = \mathrm{sign}(\xi)\frac{eE_x(0)L_Q(\xi)}{4T\cosh^2(\xi/2T)}, \tag{2.27}$$

where $E_x(0)$ is the electric field in the normal metal generating the steady current. Here we used the fact that in the stationary case $\mathbf{E} = -\boldsymbol{\nabla}\Phi/e$, which follows from Eq. (2.4). Using this relation and substituting Eqs. (2.27), (2.26) into Eqs. (2.6) and (2.24) we obtain the spatial distributions of the electric field $E_x(x)$ and the Hall current $j_y(x)$ in the superconductor,

$$E_x(x) \quad = \quad E_x(0)F_0\left(\frac{x}{\langle L_Q\rangle}\right), \tag{2.28}$$

$$j_y(x) \quad = \quad \sigma_D E_x(0)\delta_n\left(\frac{|\Delta|}{T}\right)^2 F_{-2}\left(\frac{x}{\langle L_Q\rangle}\right), \tag{2.29}$$

where $\langle L_Q\rangle = 2\ln 2(Tl/|\Delta|)$ and the functions F_n, are defined as

$$F_n(x) = \int_0^\infty dy\frac{y^n}{\cosh^2(y)}\exp\left(-\ln 2\,\frac{x}{y}\right), \tag{2.30}$$

and are plotted in Fig. 2.1. The spatial distributions of the Hall current $j_y(x)$ and the electric field $E_x(x)$ are drastically different, and cannot be related by a local Hall conductivity σ_{xy}. At relatively short distances, $l \ll x \ll \langle L_Q\rangle$, we see from Eq. (2.29) that $j_y(x) \propto \sigma_D E_x(0)\delta_n(|\Delta|/T)^2\langle L_Q\rangle/x$, so that the Hall current is

$$I_y = \int dx j_y(x) \approx \sigma_D E_x(0)\delta_n\left(\frac{|\Delta|}{T}\right)^2\langle L_Q\rangle\ln\frac{\langle L_Q\rangle}{l}.$$

2.3.4 Anomalous photo- and acousto-galvanic effects

When an electromagnetic or an acoustic wave propagates through a conductor it generates an anisotropic in momentum $\mathbf{p}$ distribution function. The induced current density is proportional to the rate of the the momentum transfer from the wave to the electron system, [29]

$$J_x = I\alpha_{xx}.$$

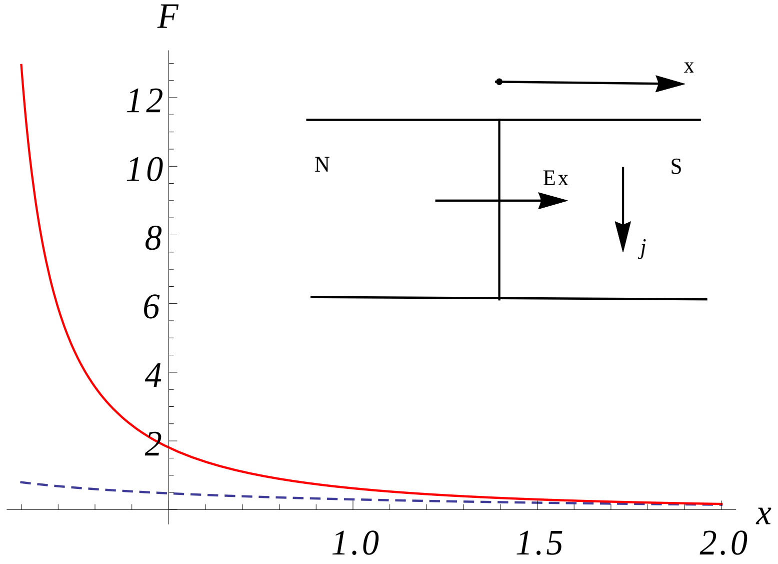

Figure 2.1: Plot of the functions $F_{-2}(x)$ (solid line) and $F_0(x)$ (dashed line) in Eq. (2.30). The inset shows a schematic setup of the normal current injection experiment. Electric current is injected into the superconductor S from the normal metal N along along the x-axis. Skew scattering of quasiparticles generates an anomalous Hall current in the y direction.

Here I is the rate of momentum density transfer due to the wave adsorption, and x is the direction of the wave propagation. In $p_x + ip_y$ superconductors an anomalous current in the y direction is generated. Considerations similar to those leading to Eq. (2.22) near T_c yield

$$\alpha_{xy} \sim \alpha_{xx} \frac{|\Delta|}{T} \, \delta_n .$$

Finally, we note that all anomalous transport phenomena discussed above are driven by the underlying symmetry of the superconducting state. Therefore they should exist in any superconductor whose order parameter breaks time reversal symmetry, see for example Refs. [36, 37, 38, 39, 40]. Although our consideration focused on $p_x + ip_y$ materials we believe our approach is applicable to other superconductors with broken time-reversal invariance.

Chapter 3

POLARIZATION-DEPENDENT PHOTOCURRENT IN POLAR STACKS OF VAN DER WAALS SOLIDS

In this chapter [1]*, we focus on the opto-elctronic transport properties of monolayers of semiconducting van der Waals solids, such as transition metal dichalcogenides (TMD). Such materials acquire significant electric polarization normal to the layers when placed on a substrate or in a heterogeneous stack. This causes linear coupling of electrons to electric fields normal to the layers. Irradiation at oblique incidence at frequencies above the gap causes interband transitions due to coupling to both normal and in-plane ac electric fields. The interference between the two processes leads to sizable in-plane photocurrent and valley current.*

3.1 Introduction

Since the discovery of graphene [41] a whole class of novel two dimensional (2D) materials, called van der Waals solids (vdWs), has been identified. [42, 43] In these 2D materials monolayers with strong in-plane bonding are coupled by weak van der Waals interactions. Few-monolayer thick structures of vdW materials have electronic and optical properties that can differ drastically from those of the bulk phases. [44] vdW materials exhibit phenomena associated with valley degrees of freedom, such as valley Hall currents [45] and valley-selective carrier photoexcitation by circularly polarized light [46], related to topological properties of the bands, such as Berry curvature and valley-dependent magnetic moment. [47] Stacking of monolayers of different vdW solids enables fabrication of novel artificial structures with interesting electronic properties. [42, 43]

In their natural form most vdW materials are nonpolar. When monolayers of different

---

[1] The material presented in this Chapter is based on Y. B. Lyanda-Geller, S. Li and A. V. Andreev, Phys. Rev. B **92**, 241406(R) (2015) , with minor alterations.

vdW materials are stacked in a heterostructure or placed on a substrate, an electric dipole moment perpendicular to the layers arises. This allows for photogalvanic effects (PGE): electric currents due to illumination by light in the absence of external electric field. In particular, a photocurrent arises between the top and bottom contacts of a heterojunction fabricated from monolayers of different vdW solids [48]. Independent of the polarization of light, This current is caused by spatial separation of photoexcited electrons and holes in a junction, and belongs to a class of effects in which the direction of the photocurrent is governed by spatial inhomogeneities of the sample or its illumination. Another class of effects, in which the direction of photocurrent or photovoltage is determined by the polarization of light [49, 50], occurs even in uniformly illuminated spatially homogeneous solids. Recently, polarization-sensitive photocurrents were observed [51] in a 2D conduction layer formed at the interface of a WSe_2 stack and the substrate was irradiated at frequencies below the band gap.

In this chapter we show that illumination of polar semiconducting vdW stacks above the band gap produces sizable polarization dependent photocurrents. They are caused by a unique asymmetry of elementary quantum processes associated with the Berry connection and the presence of a permanent electric dipole moment. Asymmetric generation of photocarriers arises from quantum interference between the conventional coupling of electrons to the in-plane ac electric field and the coupling of the permanent dipole moment to the normal component of the ac field.

In 2D structures with a dipole moment normal to the plane, polarization-dependent PGE in-plane current density, to linear order in light intensity, can be expressed in terms of a polar vector $\mathbf{d} = (0, 0, d_z)$ perpendicular to the layers by the phenomenological relation

$$\mathbf{j} = \xi\, \mathbf{d} \times i\, [\mathbf{E} \times \mathbf{E}^*] + \zeta\, [\mathbf{E}^* (\mathbf{d} \cdot \mathbf{E}) + \mathbf{E}\, (\mathbf{d} \cdot \mathbf{E}^*)]_{in}\, . \tag{3.1}$$

Here $\mathbf{E}$ is the complex electric field amplitude of a monochromatic light, subscript *in* denotes in-plane component of the vector, $\mathbf{E}(t) = \Re(\mathbf{E} e^{-i\omega t})$, and the (real) phenomenological parameters ξ and ζ describe, respectively the *circular* and *linear* PGE. In Eq. (3.1) the electric

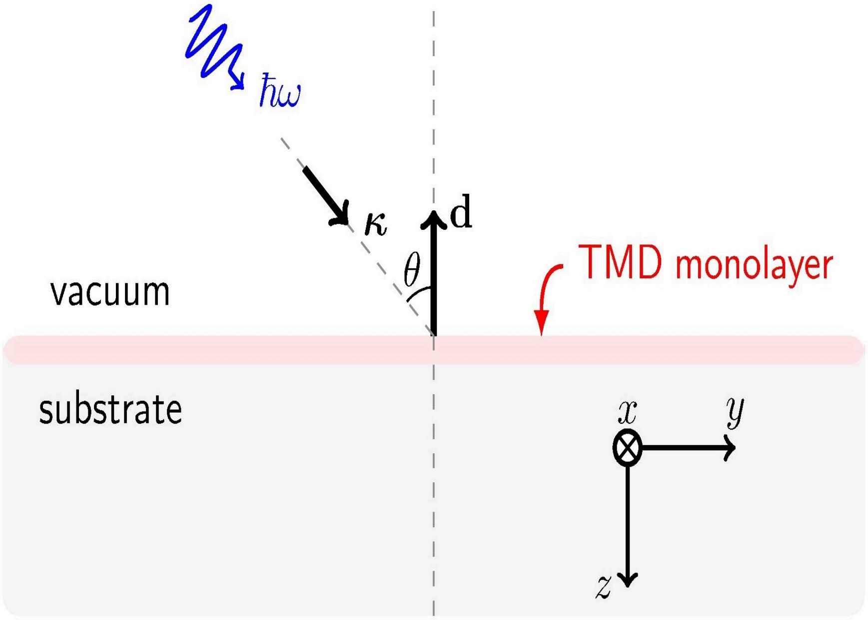

Figure 3.1: Schematic representation of the system. Irradiation of a semiconducting polar TMD monolayer by helical light at oblique incidence, $\theta \neq 0$, generates a helicity-dependent net photocurrent perpendicular to the plane of incidence yz. For linear polarization, a net current is generated in the plane of incidence.

field of the radiation is assumed spatially uniform and the photon momentum is neglected. The in-plane photocurrent arises when the sample is illuminated at oblique incidence, as shown in Fig. 3.1, and its direction and magnitude are determined by the polarization of light.

Determination of the physical mechanism of the photocurrent and evaluation of the phenomenological parameters $\mathbf{d}$, ξ and ζ in Eq. (3.1) requires a microscopic theory. The photocurrent arises due to: i) asymmetric generation of photocarriers(different generation rate for opposite electron momenta), [52, 53, 54] and ii) asymmetric kinetics (when light-induced symmetric momentum distribution leads to the current due to asymmetric scattering, due to side jumps, spin relaxation, or evolution in magnetic field). [13, 55, 56, 57, 58, 59, 60] These mechanisms adequately describe experiments that detect polarization-dependent currents in bulk semiconductors, such as Te [61] and GaAs, [62, 63, 64] and photocurrent in III-V type heterostructures [65]. Both asymmetric generation of photocarriers and kinetics play an important role in the discussion below.

When the mean free path of the photoexcited carriers exceeds their de Broglie wavelength, the photocurrent (3.1) can be expressed in terms of the electron distribution function $f_l(\mathbf{p}, \mathbf{r})$ as [13, 66, 67]

$$\mathbf{j} = e \sum_{\mathbf{p},l} \left[\mathbf{v}_l(\mathbf{p}) + \delta\mathbf{v}_l(\mathbf{p})\right] f_l(\mathbf{p}). \tag{3.2}$$

The first term here with the group velocity in a band l, $\mathbf{v}_l(\mathbf{p}) = \partial\epsilon_l(\mathbf{p})/\partial\mathbf{p}$, describes the ballistic current. The second term is the side jump (shift) current due to the displacement $\mathbf{R}_{l',l}(\mathbf{p}', \mathbf{p})$ of the center of mass of the wave packet during a transition from state $l, \mathbf{p}$ to state $l', \mathbf{p}'$ (as a result of scattering [12, 68] or photoabsorption [13, 57]). The correction to the velocity is expressed in terms of the transition probability $W_{l',l}(\mathbf{p}', \mathbf{p})$ as

$$\delta\mathbf{v}_l(\mathbf{p}) = \sum_{l',\mathbf{p}'} W_{l',l}(\mathbf{p}', \mathbf{p})\mathbf{R}_{l',l}(\mathbf{p}', \mathbf{p}). \tag{3.3}$$

The magnitude of the side jump is expressed in terms of the phase of the transition matrix element $T_{l',l}(\mathbf{p}', \mathbf{p})$ as

$$\mathbf{R}_{l',l}(\mathbf{p}', \mathbf{p}) = \mathbf{\Omega}_{l'}(\mathbf{p}') - \mathbf{\Omega}_l(\mathbf{p}) - (\partial_{\mathbf{p}} + \partial_{\mathbf{p}'}) \Im \ln T_{l',l}(\mathbf{p}', \mathbf{p}), \tag{3.4}$$

where $\mathbf{\Omega}_l(\mathbf{p})$ is the Berry connection in band l. Gauge invariance of (3.4) is obvious: When $\mathbf{\Omega}_l(\mathbf{p}) \to \mathbf{\Omega}_l(\mathbf{p}) - \partial_{\mathbf{p}}\chi_l(\mathbf{p})$, $T_{l',l}(\mathbf{p}', \mathbf{p}) \to T_{l',l}(\mathbf{p}', \mathbf{p})\, e^{i\chi_l(\mathbf{p}) - i\chi_{l'}(\mathbf{p}')}$.

In a spatially uniform steady state, and in the absence of static external electric and magnetic fields, the nonequilibrium part $\delta f_l(\mathbf{p})$ of the electron distribution function is determined by the balance between the photogeneration due to direct interband transitions $J_l(\mathbf{p})$

and relaxation and recombination of photoexcited carriers,

$$\sum_{l',\mathbf{p}'} w_{l',l}(\mathbf{p}',\mathbf{p})\,[\delta f_{l'}(\mathbf{p}') - \delta f_l(\mathbf{p})] + J_l(\mathbf{p}) = 0, \tag{3.5}$$

where $w_{l',l}(\mathbf{p}',\mathbf{p})$ is the probability of momentum relaxation[2]. Below we apply Eqs. (3.2) and (3.5) to the study of polarization-dependent currents (3.1) in polar stacks of semiconducting TMDs, such as $\mathrm{MoS_2}$ and $\mathrm{WSe_2}$.

3.2 Asymmetric generation of photocarriers

Semiconducting TMD at low number of monolayers are direct band semiconductors with strong coupling to light and sizable charge carrier mobility. [44, 47, 71] The inter-layer tunneling is weak and we neglect it. Since in this approximation the total in-plane photocurrent is the sum of contributions of individual layers, we consider the photocurrent in a single layer of TMD either placed on a substrate or in a polar stack. We assume that photon energy is not too far from the absorption threshold. In this case only electrons with momenta near the K and K' points of the hexagonal Brillouin zone absorb light and produce photocurrent, see left panel in Fig. 3.2. The effective two-band Hamiltonian for such low energy electrons is [45, 46, 72]

$$\mathcal{H} = v(\tau_z\sigma_x p_x + \sigma_y p_y) + \Delta\sigma_z, \tag{3.6}$$

where the momentum $\mathbf{p}$ is measured from the K or K' point, v has dimensions of velocity, and Δ is half the bandgap between the spin-nondegenerate conduction and valence bands. The Pauli matrices σ_i act on the band pseudospin, and τ_z acts on the valley pseudospin.

At normal incidence of the radiation, electrons couple to the in-plane component of the ac electric field. The corresponding coupling Hamiltonian is obtained from Eq. (3.6) by the usual substitution $\mathbf{p} \to \mathbf{p} - e\mathbf{A}/c$, where $\mathbf{A}$ is the vector potential and e is the electron charge. This results in valley-selective transitions for circularly-polarized light [46]; Application of an in-plane dc electric field results in valley current [45]. At oblique incidence, electrons in

---

[2] We consider light as photons resulting in quantum transitions. Photogalvanic effects have been also discussed in terms of classical high frequency electric field [55, 69, 70]

a polar stack also couple to the normal component of the ac electric field, $E_z(t)$. The full coupling of electrons to the (uniform) ac electric field is given by

$$V = -\frac{ev}{c}\left(\tau_z\sigma_x A_x + \sigma_y A_y\right) + \frac{1}{c}d_z\dot{A}_z\sigma_z, \tag{3.7}$$

where the electric field enters through the time derivative of the vector potential, $\mathbf{E} = -\dot{\mathbf{A}}/c$, and d_z is the difference between the dipole moments of electron states in the conduction and valence bands, which arises as follows. If E_z^b is a built-in electric field in a polar TMD stack, the total $z-$component of the electric field is $E_z^t = E_z^b + E_z(t)$. This electric field couples orbitals even in z, that form the conduction and valence bands described by (3.6), to odd in z higher and lower band states with energies ϵ_s, with s labeling odd bands. Then the energies of the bottom of the conduction band and the top of the valence band $\epsilon^0_{c(v)}$ change: $\delta\epsilon_{c(v)} = \sum_s |(eE_z^t z)_{c(v)s}|^2/(\epsilon^0_{c(v)} - \epsilon_s)$. Thus a coupling of charge carriers to light linear in electric field $E_z(t)$ arises, and the dipole moment difference $d_z = e^2\sum_s[(E_z^b z)_{cs}z_{sc}/(\epsilon_c^0 - \epsilon_s) - (E_z^b z)_{vs}z_{sv}/(\epsilon_v^0 - \epsilon_s)]$. This coupling plays a crucial role in generation of polarization-dependent photocurrent in vdW materials. The value of d_z can be estimated from the measured [48] dependence of the band gap on the applied external electric field perpendicular to the layers, $d_z = -d\Delta/dE_z$.

Optical transitions between the valence (-) and conduction (+) band in the K-valley are described by the matrix elements $V^K_{-+}(\mathbf{p}) = \Psi^K_+(\mathbf{p})^\dagger V \Psi^K_-(\mathbf{p})$, where the wavefunctions $\Psi^K_\pm(\mathbf{p})$ corresponding to energies $\pm\epsilon = \pm\sqrt{(vp)^2 + \Delta^2}$ are

$$\left(\Psi^K_\pm(\mathbf{p})\right)^T = \left(\pm vp_-/\sqrt{2(\epsilon \mp \Delta)\epsilon},\ \sqrt{\epsilon \mp \Delta/2\epsilon}\right). \tag{3.8}$$

Here $p_\pm = p_x \pm ip_y$, and the superscript T indicates a matrix transposition. For the K'-valley, the wavefunctions are obtained by replacing p_- in Eq. (3.8) with $-p_+$. The rate of direct optical transitions, see Fig. 3.2, in the$K$ ($j = 1$) or K' ($j = 2$) valley, assuming fully occupied valence band and empty conduction band, can be determined using the Fermi golden rule,

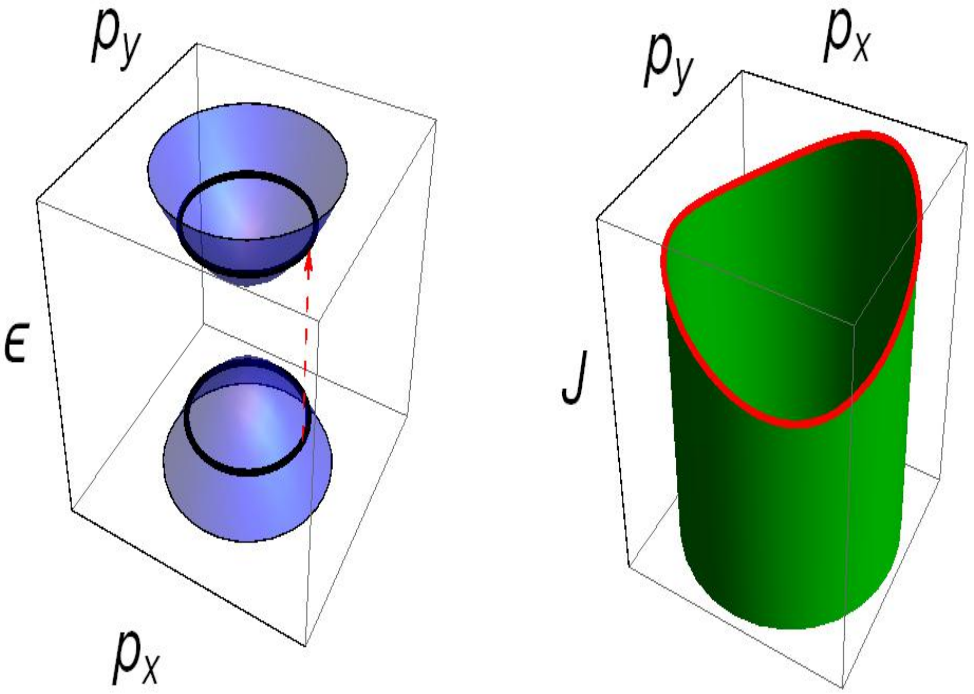

Figure 3.2: Left: Direct transitions (red arrow) between electron states in the valence and conduction bands shown for one of the valleys by black circles. Right: Asymmetric photogeneration rate.

$J_{+,j} = -J_{-,j} = J_j = \frac{2\pi}{\hbar}|V^j_{-,+}|^2\delta(\hbar\omega - 2\epsilon)$, and is given by

$$\begin{aligned} J_j(\mathbf{p}) \quad &= \frac{2\pi}{\hbar}\left(\frac{e|\mathbf{E}|v}{\omega}\right)^2 Z(p)\delta(\hbar\omega - 2\epsilon) \times \\ &\left[\frac{1-|e_z|^2}{2}\frac{\Delta^2+\epsilon^2}{\epsilon^2} - (-1)^j\kappa_z\frac{\Delta}{\epsilon} + |e_z|^2\frac{(\omega d_z p)^2}{e^2\epsilon^2}\right. \\ &-\frac{v^2}{2\epsilon^2}\left[(|e_x|^2-|e_y|^2)(p_x^2-p_y^2) + 2S_{xy}p_xp_y\right] + \\ &\left.\frac{\omega}{e\epsilon}\mathbf{p}\cdot\left(\frac{\Delta}{\epsilon}[\boldsymbol{\kappa}\times\mathbf{d}] + (-1)^j[\hat{\boldsymbol{z}}\times\hat{S}\mathbf{d}]\right)\right]. \end{aligned} \tag{3.9}$$

Here $\hat{\boldsymbol{z}}$ is the z-axis unit vector, $\mathbf{e} = \mathbf{E}/|\mathbf{E}|$ is the light polarization vector, and the pseudovector $\boldsymbol{\kappa} = i\mathbf{e}\times\mathbf{e}^*$ and the tensor $\hat{S}$, $S_{ij} = e_ie_j^* + e_i^*e_j$, characterize, respectively, the helical and the non-helical components of light polarization, with $(\hat{S}\mathbf{d})^T = (S_{xz}, S_{yz}, S_{zz})d_z$. The Sommerfeld factor [30] $Z(p)$ accounts for the Coulomb interaction between the photogenerated electron and hole. In the 2D case for a quadratic energy dispersion, $Z(p) = 2\left[1+\exp\left(-2\pi\hbar/pa_B\right)\right]^{-1}$ [73], where $a_B = \hbar^2\varepsilon/\mu e^2$ is the exciton Bohr radius, ε is the dielectric constant, p is the electron or hole momentum, and μ is the reduced effective mass. In our model, $p = \sqrt{\epsilon^2-\Delta^2}/v$, $\mu = \Delta/v^2$.

The momentum dependence of the photogeneration in Eq. (3.9) is illustrated in the right panel of Fig. 3.2. The asymmetry of photogeneration responsible for the in-plane photocurrent arises from the interference between coupling of electrons to the in-plane electric field of light and the linear Stark coupling to the normal field E_z caused by the dipole $\mathbf{d}$. It is described by the two terms linear in the electron momentum in last line of Eq. (3.9).

The different angular harmonics of the nonequilibrium distribution function relax independently. Therefore for the photocurrent it is sufficient to consider the first angular harmonic $\delta f_l^{(1)}(\mathbf{p})$ of the nonequilibrium distribution function, $\delta f_l^{(1)}(\mathbf{p}) = (\mathbf{A}_l + \tau_z\mathbf{B}_l)\cdot\hat{\mathbf{p}}$, where $\mathbf{A}_l$ and $\mathbf{B}_l$ characterize valley-even and odd asymmetry of momentum distribution, respectively, and $\hat{\mathbf{p}} = \mathbf{p}/|\mathbf{p}|$ is a unit vector along the electron momentum. The relevant scattering probability in Eq. (3.5) is given by

$$w_{l',l}(\mathbf{p}',\mathbf{p}) \to \delta_{l,l'}\left[\frac{1}{\tau_l}\hat{\mathbf{p}}\cdot\hat{\mathbf{p}}' + \tau_z\frac{1}{\tau_l^{sk}}\hat{\boldsymbol{z}}\cdot\hat{\mathbf{p}}\times\hat{\mathbf{p}}'\right], \tag{3.10}$$

where $1/\tau_l$ and $1/\tau_l^{sk}$ are respectively the transport and skew momentum relaxation rates in band l.

3.3 Photocurrent

3.3.1 Ballistic photocurrent

The first term in Eq. (3.2) for the photocurrent describes charge transfer during ballistic motion of electrons, and is characterized by the asymmetric in momentum part of the distribution function. The latter is caused by asymmetric photogeneration or subsequent asymmetric scattering. The ballistic circular PGE arises directly due to the valley-even asymmetric photogeneration (first term in the last line of Eq. (3.9)). We find that the dominant ballistic linear PGE requires a conversion, via skew scattering, of the valley-odd photogeneration (last term in Eq. (3.9)) into a valley-even asymmetric momentum distribution. Skew scattering arises only in the second Born approximation. As a result, although both transport and skew scattering rates are proportional to the impurity concentration, the skew scattering rate is smaller in the parameter $\tau_l/\tau_l^{sk} \sim \delta_l \ll 1$, where δ_l is a phase shift of electron scattering off impurities in a band l. The ballistic contribution to linear and circular PGE coefficients ξ and ζ in Eq. (3.1) are given by

$$\xi^{bal} = \left(\frac{e}{\hbar}\right)^2 \frac{Z(p_\omega)\left[(\hbar\omega)^2 - (2\Delta)^2\right]\Delta}{(\hbar\omega)^3}\,(\tau_c + \tau_v), \tag{3.11a}$$

$$\zeta^{bal} = \xi^{bal}\frac{\hbar\omega}{\Delta\,(\tau_c + \tau_v)}\left(\frac{\tau_c^2}{\tau_c^{sk}} + \frac{\tau_v^2}{\tau_v^{sk}}\right). \tag{3.11b}$$

Here τ_c and τ_v are the momentum relaxation times in the conduction and valence bands, and $p_\omega = \hbar\sqrt{E_{exc}/(\hbar\omega - 2\Delta)}/a_B$ with $E_{exc} = \mu e^4/(2\hbar^2\varepsilon^2)$ being the exciton binding energy in three dimensions.

Taking $d_z \sim 0.1$ e$\AA$, $\tau_c \sim \tau_v \sim 10^{-13}$ s (from the reported mobility 200 cm^2/(V$\cdot$ s) [71]), and the helicity $\kappa = 0.7$, we find the strength of the one monolayer circular PGE signal $\sim 10^{-8}$A/W for $\Delta = 0.9$ eV, $\hbar\omega = 1.95$ eV. This value exceeds the helicity-dependent spin-galvanic signal in 2D GaAs [65]. The ratio of the net linear PGE and circular PGE is small as τ/τ^{sk}.

3.3.2 side-jump photocurrent

Since the leading ballistic linear PGE, Eq. (3.11b), is inversely proportional to the impurity concentration, in sufficiently high mobility samples it dominates the side jump current. The side jump current, e.g., due to direct optical transitions to ζ is obtained using Eqs. (3.3), (3.4) and the expressions for $V_{-+}^{K(K')}(\mathbf{p})$. The result is

$$\zeta_{sj}^{dir} = 8\left(\frac{e}{\hbar}\right)^2 \frac{Z(p_\omega)\Delta^3}{(\hbar\omega)^3\omega}\,.$$

Other contributions to ζ stem from the asymmetry of impurity-assisted photoabsorption or from the side jumps of photogenerated carriers due to scattering off impurities, and are of the same order of magnitude as ζ_{sj}^{dir}.

3.3.3 valley photocurrent

In addition to the net current, the asymmetric photogeneration leads to the valley currents equal in magnitude but oppositely directed in the K and K' valleys, defined by $\mathbf{j}_v^{bal} = e\sum_{\mathbf{p},l}(-1)^j \mathbf{v}_{\mathbf{p},l}\delta f_l(\mathbf{p})$. The dominant ballistic contributions to circular and linear valley PGE can be found using Eqs. (3.5), (3.9) and (3.10):

$$\mathbf{j}_v^{bal} = |\mathbf{E}|^2\left[\xi^{bal}\frac{\hbar\omega}{\Delta}\left(\hat{\boldsymbol{z}}\times\hat{S}\mathbf{d}\right) + \zeta^{bal}\frac{\Delta}{\hbar\omega}\hat{z}\times[\boldsymbol{\kappa}\times\mathbf{d}]\right], \tag{3.12}$$

where ξ^{bal} and ζ^{bal} are given by Eq. (3.11). The linear and circular valley PGE are related, respectively, to the net circular (ξ^{bal}) and linear (ζ^{bal}) PGE. Therefore at $\tau_l/\tau_l^{sk} \sim \delta_l \ll 1$ the linear valley PGE is the dominant valley current that exceeds the net linear PGE valley currents flow perpendicular to the currents (3.1), similar to spin currents in the spin Hall effect. Linear valley PGE leads to accumulation of K-valley electrons at the left boundary of the monolayer with respect to the direction of the net linear PGE, and K'-valley electrons on the right. If intervalley scattering is weak, this accumulation can be measured in transport experiments [74]. Valley currents can be possibly also captured experimentally investigating non-local transport [75] or non-linear phenomena [76]. We note that polarization-dependent valley currents have been recently studied for various 2D systems including silicon channels [77] and graphene [78, 79]. In these studies, the valley currents in 2D crystals stemmed from the trigonal warping of the electron spectrum in the valleys. In our work, the mechanism of the valley current formation is based on the interference of optical transitions induced by the in-plane and out-of-plane components of the electric field of the incident light in the presence of dipole moment, and promises to yield much stronger signal.

3.3.4 Magneto-induced photocurrent

Magnetic field perpendicular to the layers, $\mathbf{H} = H\hat{\boldsymbol{z}}$, induces a Hall-like current

$$\mathbf{j}_H^{bal} = |\mathbf{E}|^2 \hat{z} \times \left[\xi_H \boldsymbol{\kappa} \times \mathbf{d} + \zeta_H \hat{S}\mathbf{d}\right]. \tag{3.13}$$

One obvious contribution to (3.13) arises from the Lorentz-force term $\frac{e}{c}\mathbf{v}_l(\mathbf{p}) \times \boldsymbol{H} \cdot \frac{\partial \delta f_l(\mathbf{p})}{\partial \mathbf{p}}$ included into the left hand side of the Boltzmann equation (3.5). The corresponding ballistic contributions ξ_H^{bal} and ζ_H^{bal} to the coefficients ξ_H and ζ_H are related to ξ^{bal} and ζ^{bal} in Eq. (3.11) by

$$\xi_H^{bal} = \xi^{bal}\omega_H(\tau_c - \tau_v),\ \zeta_H^{bal} = \frac{\zeta^{bal}\omega_H\left(\frac{\tau_c^3}{\tau_c^{sk}} - \frac{\tau_v^3}{\tau_v^{sk}}\right)}{\tau_c^2/\tau_c^{sk} + \tau_v^2/\tau_v^{sk}}, \tag{3.14}$$

where $\omega_H = 2eHv^2/\hbar\omega c$ is the cyclotron frequency.

A more interesting mechanism of magneto-induced photocurrent arises from the opposite magnetic field dependence of the band gap in the K and K' valleys; $\Delta \to \Delta \pm \mathbf{M}\cdot\mathbf{H}$, where $\mathbf{M}$ is the orbital magnetic moment in the Bloch state [80] at the K or K' points in the Brillouin zone. The latter is related to the Berry curvature [80] $\mathcal{F}_z^j(\mathbf{p}) = \partial_{p_x}\Omega_y^j(\mathbf{p}) - \partial_{p_y}\Omega_x^j(\mathbf{p})$ and in our system is given by [45, 46]

$$M_z^j = \frac{e\,\mathcal{F}_z^j(\mathbf{p})\sqrt{\Delta^2 + v^2p^2}}{\hbar c} = (-1)^j \frac{ev^2\Delta}{2\hbar c\,(\Delta^2 + v^2p^2)}. \tag{3.15}$$

The corresponding contribution to the net ballistic magneto-induced photocurrent may be expressed as

$$\mathbf{j}_m = M_z H \hat{\boldsymbol{z}} \times \frac{\partial \mathbf{j}_v^{bal}}{\partial \Delta}, \tag{3.16}$$

where $\mathbf{j}_v^{bal}$ is the magnitude of the $H = 0$ ballistic valley current (3.12). The magnetic moment contribution (3.16) is $\sim \mathbf{j}_v^{bal} \hbar\omega_H/(\hbar\omega - 2\Delta)$, while the Lorentz force contribution to linear PGE (3.14) is $\sim \mathbf{j}_v^{bal} \omega_H \tau_l^2/\tau_{sk}$. The ratio of $\mathbf{j}_m$ to linear PGE in Eq. (3.1) at $H = 0$ is $\hbar\omega_H \tau_{sk}/[(\hbar\omega - 2\Delta)\tau]$, which can easily reach $\sim \omega_H \tau$, usually defining the Lorentz force effects. The role of (3.16) is further enhanced by the partial cancellation between the Lorentz force contributions of electrons and holes to linear and circular PGE in Eq. (3.14), and the magnetic moment contribution may become the dominant magneto-induced photocurrent in lower mobility samples.

3.4 Discussion

Besides polar TMD systems, our approach based on Eqs. (3.6) and (3.7) may be used to study linear and circular PGE induced by interband transitions in polar boron nitride structures. Another interesting system is a Bernal stacked graphene bilayer placed on a substrate [81], in which the photocurrents predicted here can potentially be tuned by gating the system. Helicity-dependent photocurrents in single layer graphene were observed in Ref. [82]. The existence of such photocurrents induced by an in-plane external magnetic field and Rashba-like spin-orbit effects [83, 84, 85] was recently suggested in graphene [86]. We expect that photocurrents in polar bilayer graphene, caused by the coupling of light to the orbital dipole moment $\mathbf{d}$, will be significantly larger. The photogalvanic effects dependent on polarization of light originate from asymmetry of elementary quantum mechanical processes, such as photogeneration, scattering or recombination, spin relaxation or precession, or combined processes, in which optical transitions are accompanied by scattering to generate asymmetry of photoexcitation. Mechanisms associated with pure asymmetry of scattering, spin-relaxation or precession are rather interesting because optical excitation is separate from the stages when the current is generated. This creates the possibility to separate time scales which characterize generation of the current. Usually, situations that resulted in such physics were characterized by photogeneration symmetric in charge carrier momentum, and asymmetry arised on consequent stages. We observe in this work that van der Waals dichalcogenides represent an unusual physical situation. Here, in the linear PGE, the photocurrent associated with skew valley scattering arises due to photogeneration that is asymmetric both in momentum and in valley index, while symmetric photogeneration due to interband optical transitions does not lead to further contributions. This makes mechanisms of linear PGE similar to mechanisms of anomalous (and spin) Hall effects.Indeed, there are contributions to all these phenomena, e.g., from skew scattering or side jump mechanisms. It is important to mention, however, that anomalous and spin Hall effects mostly arise accompanied by spin relaxation, which often makes identification of individual mechanisms difficult. Transitions between valleys in dichalcogenides, and their time scales, substantially differ from spin relaxation processes. They also differ from elementary processes in other photogalvanic settings, in which current due to scattering asymmetry arises due to symmetric in momentum photogeneration. This peculiarity of van der Waals dichalcogenides and similar systems may potentially open interesting avenues in investigation of side jump effects and related phenomena.

Chapter 4

SPIRALING FERMI ARCS IN WEYL MATERIALS

In Weyl materials the valence and conduction electron bands touch at an even number of isolated points in the Brillouin zone. In the vicinity of these points the electron dispersion is linear and may be described by the massless Dirac equation. This results in nontrivial topology of Berry connection curvature. One of its consequences is the existence of peculiar surface electron states whose Fermi surfaces form arcs connecting projections of the Weyl points onto the surface plane. Band bending near the boundary of the crystal also produces surface states. We show that in Weyl materials band bending near the crystal surface gives rise to spiral structure of energy surfaces of arc states. The corresponding Fermi surface has the shape of a spiral that winds about the projection of the Weyl point onto the surface plane. The direction of the winding is determined by the helicity of the Weyl point and the sign of the band bending potential. For close valleys arc state morphology may be understood in terms of avoided crossing of oppositely winding spirals.[1]

4.1 Introduction

The possibility of existence of zero band gap semiconductors with linear electron dispersion near the contact points of conduction and valence bands in the Brillouin zone and the stability of this state with respect to Coulomb interactions has been investigated extensively beginning with the work of Abrikosov and Beneslavskii [87]. Recently there has been a renewal of theoretical [88, 89, 90, 91, 92, 93, 94, 95, 96, 97, 98, 99, 100, 101] and experimental research [102, 103, 104, 105, 106, 107, 108, 109] on Weyl meterials, in which the electron

---

[1] The material presented in this Chapter is based on S. Li and A. V. Andreev, Phys. Rev. B **92**, 201107(R) (2015) , with minor alterations.

dispersion near the point of crossing of the two non-spin-degenrate bands corresponds to that of relativistic massless (Weyl) fermions. The corresponding Berry connection curvature [3] is divergence free with the exception of the band contact points, where monopole "charges" are located. By Nielsen and Ninomiya [110, 111] such Weyl point come in pairs of opposite helicity. In Weyl materials the Adler-Bell-Jackiw chiral anomaly, [112, 113] first discovered in particle physics, may be realized. This gives rise to giant anisotropic negative magnetoresistance. [98, 103, 104, 110, 111]

Weyl materials possess surface states [89, 95] whose Fermi surfaces have the shapes of arcs connecting the projections of the Weyl points onto the crystal plane of the surface. Their origin is also rooted in the nontrivial topology of the Berry phase connection. [101] Arc states are close relatives of chiral edge states in graphene. [114, 115, 116] The latter also owe their existence to the structure of Berry curvature in graphene, [116], and their spectrum (as a function of momentum along the edge) consists of a line connecting the projections of the two Dirac points onto the edge. Evidence for arc states was recently observed by angle resolved photoemission spectroscopy (ARPES) in several Weyl materials. [105, 106, 107, 108, 109]

Another common mechanism of surface state generation is band bending. It is caused by the difference between electron environments at the surface and in the bulk. In previous theoretical considerations of arc states breaking of particle-hole symmetry due to band bending near the surface was ignored (breaking of particle-hole symmetry at the graphene boundary leads to a finite dispersion of these, otherwise dispersionless, surface states. [117, 118, 119]) The resulting energy dispersion of arc states is depicted in Fig. 4.1.

In this chapter we study the effects of band-bending near the surface of Weyl materials. For conventional semiconductors surface states caused by band bending are characterized by closed Fermi surfaces, see right panel in Fig. 4.2. We show that in Weyl materials surface states caused by band bending hybridize with the arc states to form a single band with spiraling energy dispersion, shown in the left panel of Fig. 4.2. The corresponding Fermi surface is shaped as a spiral that winds about the projection of the Weyl points onto the boundary, see the left panel of Fig. 4.4.

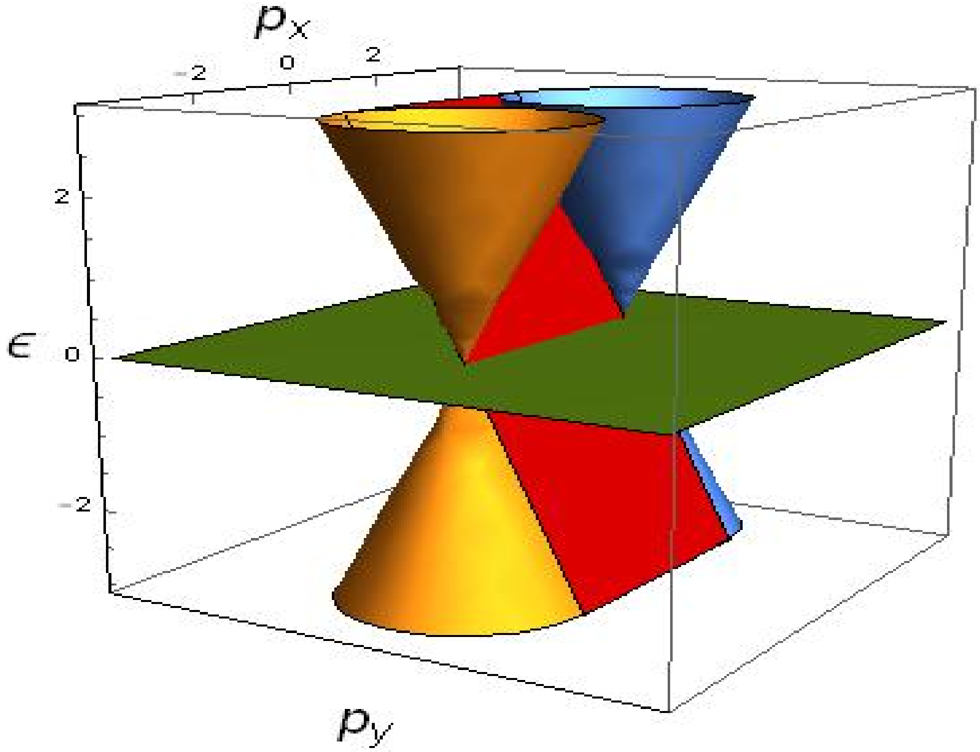

Figure 4.1: Sketch of the energy dispersion of the bulk states (interior of the Dirac cones) and the surface arc states (inclined plane segment) in the absence of band bending.

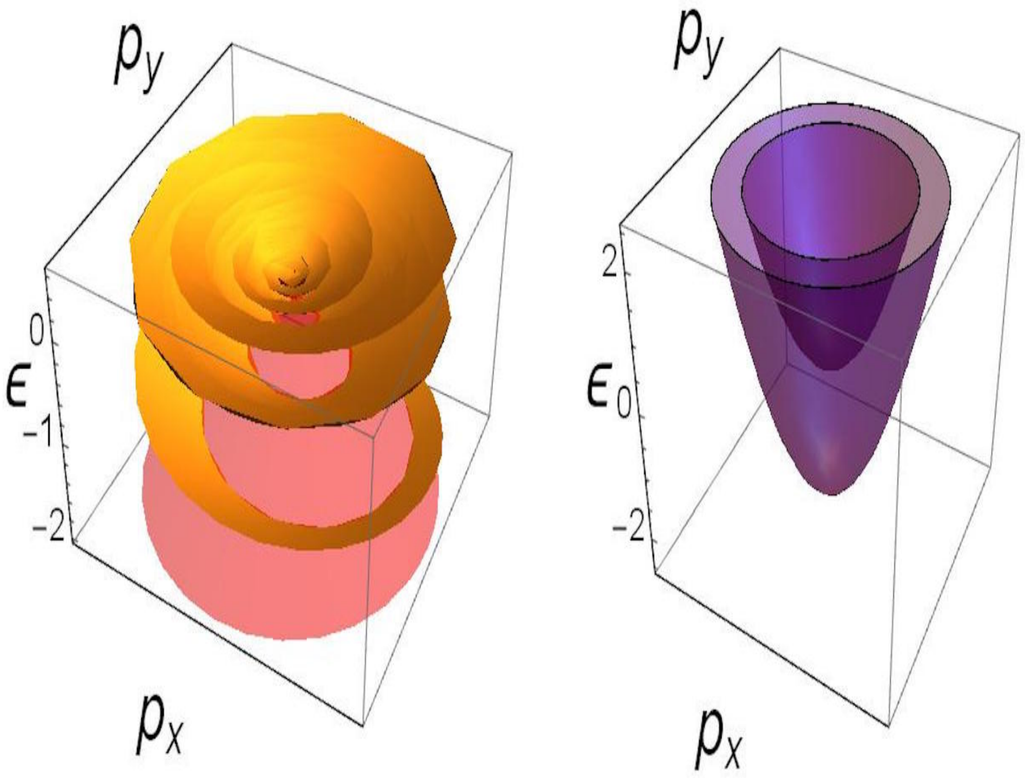

Figure 4.2: Left: the spiral energy surface of bound states for band bending potentials obtained from Eq. (4.7) with parameters $\gamma = 4.5,\ z_0 = 0.01$. For clarity only the part with $\theta \in (-\pi/2, \pi/10)$ is shown. The surface terminates at the Dirac cones of particle-like and hole-like states of the continuum. Right: parabolic energy surfaces of bound states for a conventional semiconductor.

4.2 Spiraling energy dispersion of surface arc states of a single Weyl point

We consider a crystal boundary perpendicular to the z-axis, as illustrated in Fig. 4.3. In the two band approximation an electron state with a fixed crystalline momentum parallel to the boundary, $\mathbf{p}$, may be described by a two-component pseudospinor,

$$\psi_{\mathbf{p}}(z) = \begin{pmatrix} u_{\mathbf{p}}(z) \\ v_{\mathbf{p}}(z) \end{pmatrix}.$$

Assuming for simplicity of presentation an isotropic [2] dispersion near the Weyl points we write the effective low energy Hamiltonian in the form

$$\hat{H} = U(z) + v\mathbf{p}\cdot\boldsymbol{\sigma} - i\hbar v\partial_z\sigma_z. \tag{4.1}$$

Here $\mathbf{p} = (p_x, p_y)$ and $\boldsymbol{\sigma}$ are Pauli matrices, and the band bending is described by the potential $U(z)$. The eigenstates with energy ϵ obey the corresponding Dirac equation,

$$\begin{pmatrix} \epsilon + i\hbar v\partial_z - U(z) & -vp \\ -v\bar{p} & \epsilon - i\hbar v\partial_z - U(z) \end{pmatrix}\begin{pmatrix} u_{\mathbf{p}}(z) \\ v_{\mathbf{p}}(z) \end{pmatrix} = 0, \tag{4.2}$$

where $p = p_x - ip_y$, and $\bar{p} = p_x + ip_y$.

In a general situation the projections of different Weyl points onto the plane of momentum parallel to the boundary do not coincide. In this case the boundary conditions do not couple different valleys and can be parameterized by a single phase χ,

$$\left(v_{\mathbf{p}} - e^{i\chi}u_{\mathbf{p}}\right)\Big|_{z=z_0} = 0. \tag{4.3}$$

This corresponds to a vanishing current normal to the boundary, $j_z = v\psi^\dagger\sigma_z\psi$. [117, 119]

The pseudospinor amplitudes obey second order differential equations, i.e.

$$u''_{\mathbf{p}}(z) + \left\{\left[\frac{\epsilon - U(z)}{\hbar v}\right]^2 + i\frac{U'(z)}{\hbar v} - \frac{|\mathbf{p}|^2}{\hbar^2}\right\}u_{\mathbf{p}}(z) = 0. \tag{4.4}$$

Here the derivative with respect to z is denoted by prime. As follows from (4.2) the v amplitude may be obtained from the u amplitude by a differential operation

$$pv_{\mathbf{p}}(z) = \left[\epsilon - U(z) + i\hbar v\partial_z\right]u_{\mathbf{p}}(z). \tag{4.5}$$

The momentum dispersion of states bound to the surface, $\epsilon(\mathbf{p})$, is determined by discrete spectrum of the operator in Eq. (4.1) with the boundary condition Eq. (4.3). Although our conclusions regarding the spiral structure of the dispersion of surface states, $\epsilon(\mathbf{p})$, are

---

[2] Accounting for the anisotropy of the Dirac cones does not change our conclusions

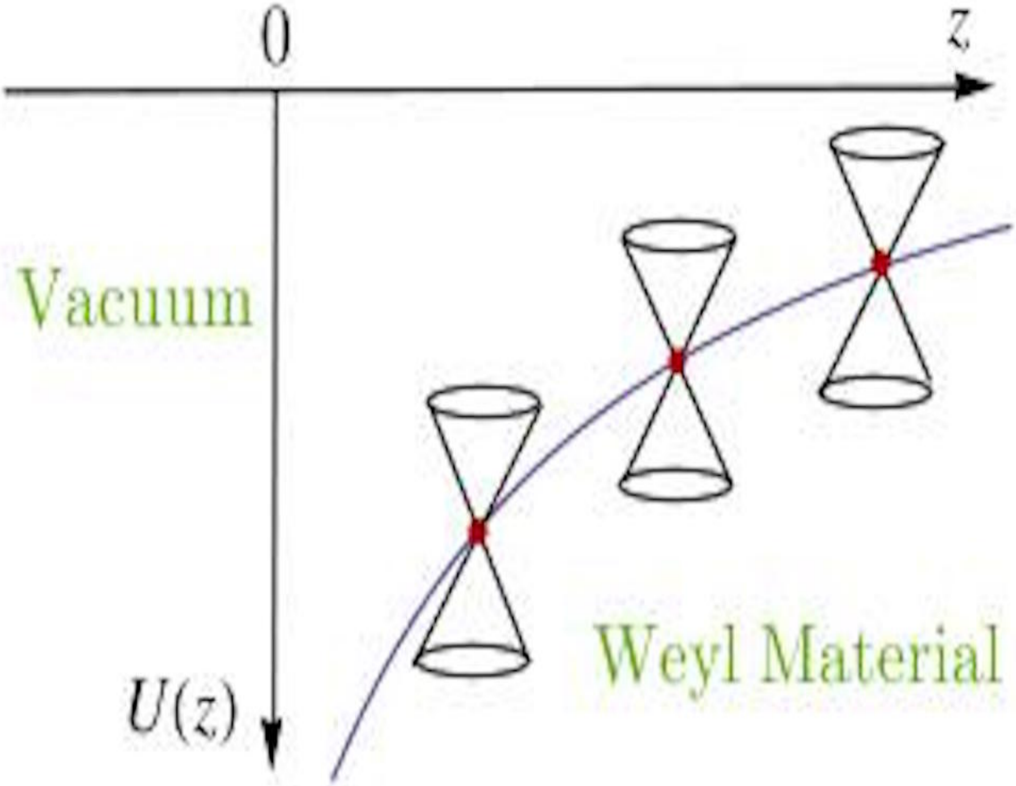

Figure 4.3: Schematics of band bending potential $U(z)$ and Weyl cones close to the boundary.

quite general, the specific shape of the dispersion depends on the details of the band-bending potential.

The energy dispersion relation near the boundary of the continuum depends on the long (as compared to the lattice constant) distance behavior of the potential $U(z)$. The corresponding macroscopic electric fields are created by the double layer charge distribution near the surface and depend on the screening properties of the Weyl material. In this respect one needs to distinguish between two cases: i) For zero band gap semiconductors at zero temperature, $T = 0$, linear screening is absent and $U(z)$ is expected to decay as a power of z, ii) For zero band gap semiconductors at finite temperature or semimetals,[3] $U(z)$ decays exponentially at distances greater that the screening length (which is much longer than the lattice constant). In either of these cases the spatial dependence of $U(z)$ at long distance may be analyzed using the Poisson's equation, $U''(z) = -4\pi e^2 n(z)$, where e is the electron charge and $n(z)$ is the density of electrons.

4.2.1 Semiconducting case

In this case the thermodynamic electronic density of states (compressibility) $\partial n/\partial\mu$ vanishes in the bulk for an undoped system. As a result, linear screening is absent, and the potential $U(z)$ exhibits a power law fall off with the distance z from the boundary.

For small coupling constants, $\alpha = e^2/\hbar v$, the band-bending region near the surface hosts many bound states. In this case the spatial dependence of the electron density may be determined using the Thomas-Fermi approximation. In the undoped crystal the electrochemical potential is measured with respect to the Weyl point, i.e. $U(z) + \mu(z) = 0$. Due to the linear dispersion the electron density depends on the local potential $U(z)$ as $n(z) = -gU(z)^3/3\pi^2\hbar^3 v^3$, where g is the number (even) of the Weyl points in the Brillouin

---

[3] To avoid confusion we note that following the traditional nomenclature we use the term semimetals for materials in which the zero temperature densities of electrons and holes are finite and equal to each other. In a Weyl material this corresponds to energy offset of some Weyl valleys relative to others, causing partial band overlap. The semiconducting case refers to materials with no energy offset between different valleys. In the literature on Weyl materials, in contrast to the conventional terminology, these two cases are often referred to as respectively Weyl metals and Weyl semimetals.

zone. This yields the Thomas-Fermi equation in the form

$$U''(z) = \frac{4g\alpha}{3\pi(\hbar v)^2} U^3(z). \tag{4.6}$$

The relevant solution is given by

$$U(z) = \hbar v \frac{\gamma}{z}, \quad |\gamma| = \sqrt{\frac{3\pi}{2g\alpha}} \gg 1. \tag{4.7}$$

The short-distance behavior of the confining potential may not be understood within the low energy framework employed here and is accounted for by the boundary condition (4.3), which should be imposed at distance of the order of the lattice constant.

The second order differential equation Eq. (4.4) with the potential $U(z)$ given by Eq. (4.7) can be reduced to the equation for the confluent hypergeometric function. Introducing the dimensionless variable $\zeta = 2\sqrt{|\mathbf{p}|^2 - (\epsilon/v)^2}\; z/\hbar$ we can write the general solution of Eq. (4.4) in the form

$$u(\zeta) = \zeta^{-i\gamma} \exp(-\zeta/2) w(\zeta), \tag{4.8}$$

were $w(\zeta)$ is expressed in terms of the confluent hypergeometric function $\Phi(a, c\,; \zeta)$ [120] as

$$w(\zeta) = \Phi\left(a, c\,; \zeta\right) + C_1\, \zeta^{1-c} \Phi\left(a - c + 1, 2 - c\,; \zeta\right) \tag{4.9}$$

with $a = \gamma\left(\epsilon/\sqrt{v^2|\mathbf{p}|^2 - \epsilon^2} - i\right)$, and $c = -2i\gamma$.

For bound states the value of the constant C_1 is determined from the condition that the wavefunction decay exponentially at $\zeta \to \infty$. Using the large distance asymptotic of $\Phi(a, c\,; \zeta)$, we find

$$C_1 = \frac{a^*}{c(1-c)} \frac{\Gamma(a^*)}{\Gamma(a)} \frac{\Gamma(c)}{\Gamma(c^*)}, \tag{4.10}$$

where $\Gamma(x)$ is the gamma function. The spectrum of surface states is determined by substituting this form of u given by Eqs. (4.8)-(4.10) into Eq. (4.5) and using the boundary condition, Eq. (4.3). Since the latter is imposed at short distances $z = z_0 \ll \hbar/|\mathbf{p}|$, which corresponds to $\zeta_0 \ll 1$, the result of this substitution simplifies to

$$e^{i\left(\phi - \theta - \frac{\pi}{2}\right)} \frac{\Gamma(a^*)\Gamma(c)}{\Gamma(a)\Gamma(c^*)}\, e^{2i\gamma \ln\left(\frac{2|\mathbf{p}|z_0}{\hbar} \cos\theta\right)} = e^{i\chi}. \tag{4.11}$$

Here $a = \gamma(\tan\theta - i)$, and we parameterized the energy of bound states, $|\epsilon| < v|\mathbf{p}|$, by the angle θ, so that $\epsilon = v|\mathbf{p}|\sin\theta$, with $\theta \in (-\pi/2, \pi/2)$, and introduced the momentum azimuthal angle ϕ, $\mathbf{p} = |\mathbf{p}|(\cos\phi, \sin\phi)$.

Eq. (4.11) has a clear interpretation. Vanishing of the normal current $j_z = v\psi^\dagger\sigma_z\psi$ in a stationary state implies that the ratio $v_{\mathbf{p}}(z)/u_{\mathbf{p}}(z)$ is a pure phase factor. The condition of exponential decay of the solution at $z \to \infty$ requires that $v_{\mathbf{p}}(z)/u_{\mathbf{p}}(z)|_{z\to\infty} = e^{i\left(\phi+\theta-\frac{\pi}{2}\right)}$. The remaining factor in the left hand side of Eq. (4.11) describes the dynamical phase accumulated during the motion between the boundary and $z \to \infty$. By the boundary condition (4.3) the product of these phase factors must be equal to $e^{i\chi}$ in the right hand side.

In the absence of the band bending potential the dynamical phase vanishes. In this case bound states exist only in half the momentum plane, ϕ-$\chi \in (0, \pi)$, in agreement with the treatments ignoring the band bending effects near the crystal surface. At $\gamma \neq 0$ the dynamical phase accumulated due to the presence of the band bending potential allows the phase difference ϕ-χ to depart from the interval $(0, \pi)$ and produces the spiraling structure of the energy surface. By Levinson's theorem [30] this phase is given by 2π times the number of bound states in the corresponding confining potential. As a result, the number of turns made by the spiraling energy surface around $|\mathbf{p}| = 0$ is equal to the number of bound states caused by band bending.

Due to the slow $1/z$ fall off, the potential in Eq. (4.7) hosts an infinite number of shallow bound states. This is reflected in the logarithmic divergence of the phase on the left hand side of Eq. (4.11) at small parallel momenta, $|\mathbf{p}| \to 0$. The shape of the Fermi surface of bound states in an undoped Weyl material is determined by setting $\theta = 0$ (zero energy) in Eq. (4.11). The resulting spiral, which makes an infinite number of turns in the p_x-p_y plane, is plotted in the left panel of Fig. 4.4.

The spectrum of bound states with nonzero energy is given by Eq. (4.11) with $\theta \neq 0$. For each momentum $\mathbf{p} = |\mathbf{p}|(\cos\phi, \sin\phi)$ it yields a discrete spectrum of bound states. This defines a surface in three dimensional space with coordinates p_x, p_y and ϵ. In order to visualize this surface we can view Eq. (4.11) as the expression for the azimuthal angle ϕ as

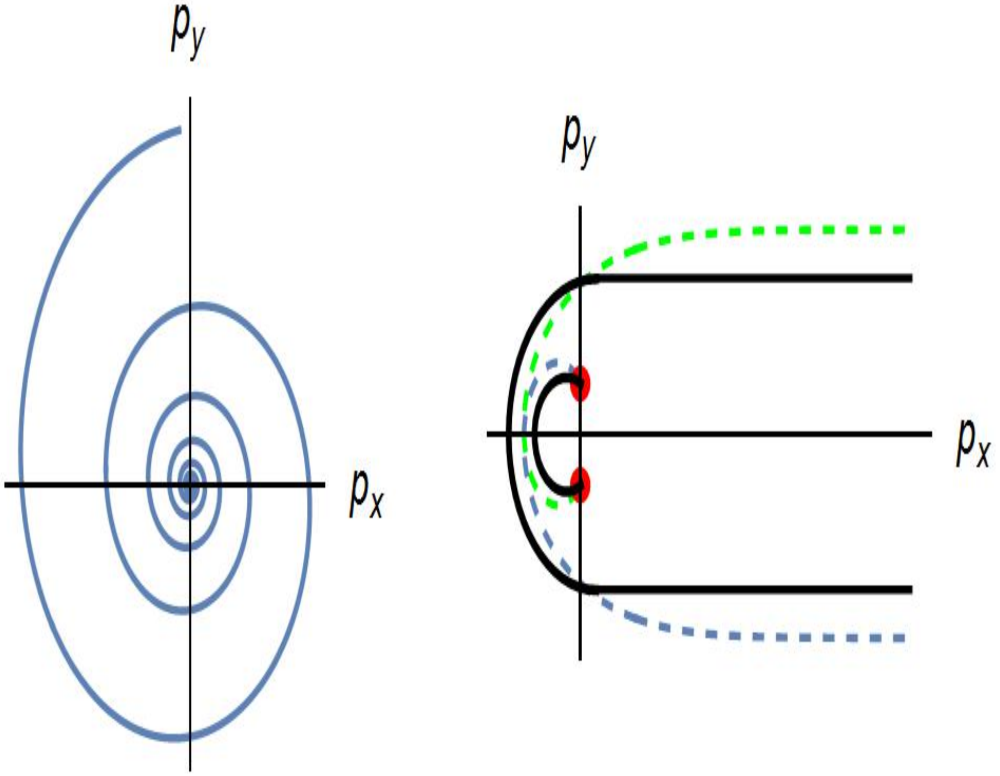

Figure 4.4: Left: Fermi arc shape for the undoped Weyl semiconductor determined from Eq. (4.11). The spiral makes infinite number of turns about the Weyl point. Right: Dashed lines – Fermi arc shapes for two nearby valleys of opposite helicity for a square well potential, Eq. (4.12). The spirals make a finite number of turns (equal to the number of the bound states) about the Weyl points (red dots). Solid lines – avoided crossing of the two spirals due to finite valley mixing.

a function of energy (θ) and the absolute value of momentum $|\mathbf{p}|$. This gives a parametric representation of the dispersion relation of bound states. A three dimensional parametric plot of $p_x = |\mathbf{p}|\cos\phi$, $p_y = |\mathbf{p}|\sin\phi$ and $\epsilon = v|\mathbf{p}|\sin\theta$ as a function of two parameters, $|\mathbf{p}| > 0$ and $\theta \in (-\pi/2, \pi/2)$ that follows from Eq. (4.11) is presented in the left panel of Fig. 4.2.

4.2.2 Semimetallic case

For potentials $U(z)$ that decay faster than $1/z$ into the bulk the number of bound states is finite. Therefore, the spiral Fermi surface makes a finite number of turns about the $\mathbf{p} = 0$ point. As an illustration we consider the simplest example of such a potential, a square well of depth U_0, $U(z) = -U_0\theta(z_0 - z)$. The treatment of this case as outlined above is straightforward and leads to the following counterpart of Eq. (4.11),

$$e^{i\left(\phi+\theta-\frac{\pi}{2}\right)}\,\frac{q + (|\mathbf{p}|\cos\theta/\hbar + i\tilde{U})\tan(qz_0)}{q + (|\mathbf{p}|\cos\theta/\hbar - i\tilde{U})\tan(qz_0)} = e^{i\chi}, \tag{4.12}$$

where $\tilde{U} = U_0/\hbar v$ is measured with respect to wave vector and

$$q = \sqrt{\tilde{U}^2 + 2\tilde{U}|\mathbf{p}|\sin\theta/\hbar - (|\mathbf{p}|\cos\theta/\hbar)^2},$$

with the same parameterization as before. The shape of the Fermi surface can be obtained by setting θ to 0 in Eq. (4.12) and is plotted in the right panel of Fig. 4.4. The number of windings it makes in the $p_x - p_y$ plane is set by the number of bound states in the well, $\propto \tilde{U}z_0$. The characteristic momentum scale p_s of the spiraling region is set by the depth of the well, $p_s \approx U_0/v$.

Note that the direction of the winding of the spiraling energy surface is opposite for the opposite helicity of the Weyl point or opposite sign of the band bending potential. Thus for a known valley helicity the winding direction of the spiraling arc may be used to infer the sign of the band bending potential.

4.3 Spiraling energy dispersion of surface arc states of two close Weyl points

The Fermi arcs join Weyl valleys with opposite helicity. If the momentum scale of the helical structure, $p_s \approx U_0/v$ is smaller than the momentum distance Δp between the (projections on the terminating surface) Weyl points then the spiral structures near each valley bay be considered independently, as above. In the opposite case, $p_s \leq \Delta p$ the interaction between the valleys becomes important. In many of the Weyl materials Weyl valleys form nearby pairs with intervalley distance Δp significantly smaller than the Brillouin zone size. In this case the effect of the intervalley interaction on the helical structure of arc states may be studied using the Dirac equation. Valley mixing of surface states arises from: i) valley coupling in the bulk, and ii) intervalley scattering from the crystal surface. The first effect is captured by the four band Dirac Hamiltonian, so that Eq. (4.1) may be replaced with [93, 91, 92] $\hat{H} = U(z) + v\tau_3\mathbf{p}\cdot\boldsymbol{\sigma} + \Delta\tau_1\sigma_x$ with $\boldsymbol{\tau}$ being the Pauli matrices in the valley subspace. In this formulation the current operator becomes $\mathbf{j} = ev\Psi^\dagger\tau_s\boldsymbol{\sigma}\Psi$. The intervalley scattering at the boundary is accounted for by generalizing the boundary condition (4.3) that corresponds to the vanishing of the current j_z normal to the boundary,

$$\vec{v}_\mathbf{p} = \hat{M}\vec{u}_\mathbf{p}. \tag{4.13}$$

Here $\vec{u}_\mathbf{p}$ and $\vec{v}_\mathbf{p}$ are the two component (in the valley subspace) generalizations of the spinor amplitudes $u_\mathbf{p}$ and $v_\mathbf{p}$, and $\hat{M}$ is a 2×2 unitary matrix whose nondiagonal elements describe intervalley scattering from the boundary. In the absence thereof the matrix reduces to the diagonal form (4.3), $M_{ij} = \delta_{ij}e^{i\chi_j}$.

In the absence of valley mixing the arc states form two intersecting spirals winding in opposite directions (due to the opposite helicity of the Weyl valleys), shown in the solid lines in the right panel in Fig. 4.4. Arc state morphology at weak mixing may be understood in terms of avoided crossing of these spirals. It yields two alternative morphologies of arc states Fermi surfaces. Type I – all Fermi lines confined to the vicinity of the pair of the Weyl nodes (with one arc connecting them and, possibly one or more closed lines nearby). Type II – a pair of arcs emanating from the coupled Weyl nodes to other Weyl pairs. In the four band Dirac model both cases are realized depending on the choice of parameters in the Hamiltonian and the boundary condition (4.13).

To illustrate the effects of valley mixing let us for simplicity neglect the valley coupling Δ in the bulk. In this case the ratio of the spinor amplitudes $v^j_{\mathbf{p}}/u^j_{\mathbf{p}}$ in valley j is a pure phase factor. For the potentials we considered, its value at the boundary, $e^{i\alpha^j_{\mathbf{p}}}$, is given by the left hand side in Eqs. (4.11) and (4.12) [4]. Thus, according to the boundary condition (4.13) the spectrum of arc states is determined by the equation $\det\left[\delta_{ij}e^{i\alpha^j_{\mathbf{p}}} - M_{ij}\right] = 0$. Parameterizing the matrix $\hat{M}$ in Eq. (4.13) as $\hat{M} = e^{i\chi}e^{i\tau_2\Theta}$, where the angle Θ describes the valley mixing, and χ is the phase characterizing the intra-valley reflection, c.f. Eq. (4.3), and using the phase factors $e^{i\alpha^j_{\mathbf{p}}}$ for the square well potential, Eq. (4.12) we get the energy dispersion of mixed valleys. At zero valley mixing, $\Theta = 0$ the Fermi arcs are shown by the dashed lines in the right panel of Fig. 4.4. Avoided crossings due to small valley mixing results in type II morphology (solid lines), which is consistent with "tadpole" arc shape observed in Refs. [105, 106, 107, 108, 109].

In summary, we studied the interplay between the conventional, band bending mechanism of surface state formation, and the topological mechanism leading to formation of arc states. It results in a spiral structure of energy dispersion of surface states near the Weyl nodes. For close valleys, the arc state morphology may be understood in terms of avoided crossing of the spirals of individual valleys. Our findings significantly affect the density and the dynamics of electrons in the surface metallic channel.

---

[4] Note that the azimuthal angle ϕ and $|\mathbf{p}|$ in each valley should be determined relative to the corresponding Weyl node.

Chapter 5

KLEIN TUNNELING AND MAGNETORESISTANCE OF *P-N* JUNCTIONS IN WEYL SEMIMETALS

We follow the transport study in Weyl semimetals in this chapter [1]*. Specifically, we are interested in the zero temperature conductance and magnetoconductance of ballistic p-n junctions in Weyl semimetals. Electron transport is mediated by Klein tunneling between n- and p- regions. The chiral anomaly in Weyl semimetals plays a crucial role in the magnetoconductance of the junction. With the exception of field orientations where the angle between* $\mathbf{B}$ *and the junction plane is small, magnetoconductance is positive and linear in* B *at both weak and strong magnetic fields. In contrast, magnetoconductance in conventional p-n junctions is always negative.*

5.1 Introduction

A theory of low temperature resistance and magnetoresistance (MR) of *p*-*n* junctions in conventional semiconductors was developed long ago [121, 122, 123]. The junction conductance is determined by tunneling processes of electrons between the conduction and valence bands in the presence of the built-in electric field of the junction. In this case the MR is positive, and becomes exponentially large at strong magnetic fields B. Two- and one-dimensional *p*-*n* junctions in semiconductors with a gapless Dirac spectrum $\varepsilon_{\mathbf{p}} = \pm v|\mathbf{p}|$ (v is the velocity of electrons) can be realized in graphene [124, 125, 126], armchair carbon nanotubes [127, 128] and on the surface of topological insulators [129]. The main difference with conventional semiconductors is that in the gapless case the junction conductance is dominated by Klein tunneling; electrons near normal incidence are transmitted through the junction without

---

[1] The material presented in this Chapter is based on S. Li, A. V. Andreev and B. Z. Spivak, Phys. Rev. B **94**, 081408(R) (2015) , with minor alterations.

backscattering. As a result, at $B = 0$ the conductance of a graphene p-n junction is proportional to the square root of the built-in electric field E of the junction, $G \sim \frac{e^2}{h}\frac{W}{l_E}$. Here W is the width of the junction and $l_E = \sqrt{\hbar v/|e|E}$ is the characteristic length determined by the built-in electric field E. In a finite magnetic field perpendicular to the graphene sheet the MR of the junction is positive [125] and becomes exponentially large at large B.

Recently a new class of three-dimensional materials (Weyl semimetals) was discovered [89, 92, 94, 95, 96, 103, 108, 130, 131, 132, 133, 134, 135, 136, 137, 138], in which dynamics of low energy electrons in valley i may be described by a gapless Dirac Hamiltonian

$$H_i = \chi_i v\, \boldsymbol{\sigma} \cdot \mathbf{p} + \Delta_i + U(\mathbf{r}). \tag{5.1}$$

Here $\chi_i = \pm 1$ is the valley chirality, $\boldsymbol{\sigma} = (\sigma_x, \sigma_y, \sigma_z)$ are the Pauli matrices, $\mathbf{p}$ is the momentum measured from the Weyl node, Δ_i is the energy offset of the Weyl node from the chemical potential in an undoped crystal, and $U(\mathbf{r})$ is the potential energy. Due to the Nielsen-Ninomiya theorem [110, 111] the number of the Weyl nodes, g, in the Brillouin zone must be even, and the number of opposite chirality nodes should be equal. The stability of the Weyl nodes is related to the fact that the flux of Berry curvature through a closed surface surrounding the node is quantized. Since the time reversal symmetry requires the Berry curvature to be an odd function of momentum and inversion symmetry requires it to be even, Weyl nodes can only exist in crystals with either broken inversion or time reversal symmetry. In the former case the minimal number of Weyl nodes is four, while in the latter case it is two. An interesting property of Weyl fermions is the existence of chiral (zeroth) Landau levels in a magnetic field. This feature is related to the chiral anomaly [110, 111, 112, 113] and leads to a strong anisotropic MR [98, 110, 111, 139] in these materials. In this Letter we study the conductance and magnetoconductance of a p-n junction in a Weyl semimetal. We show that the interplay between the chiral anomaly and and Klein tunneling results in negative MR of the junction.

The specific geometry of the junction is shown in the inset of Fig. 5.1. Doping in the p- and n- regions creates a built-in electrostatic potential $U(z)$. Similar to graphene p-n

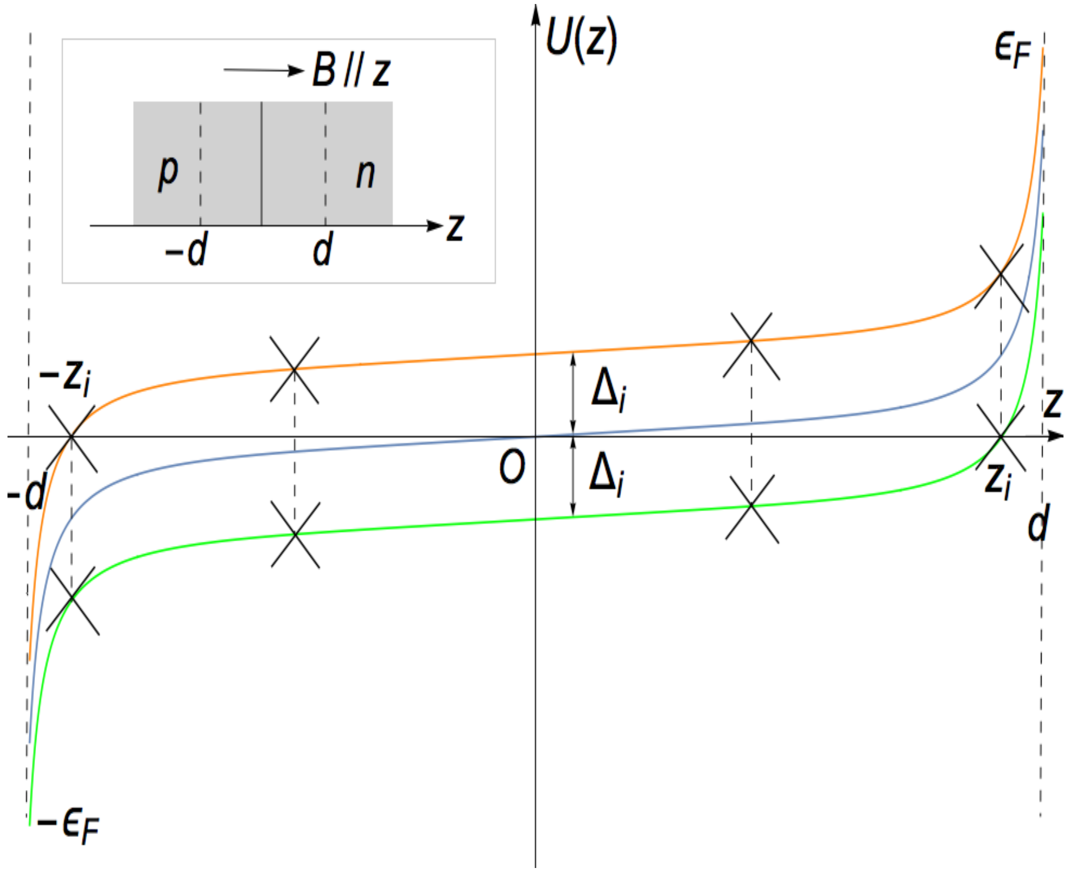

Figure 5.1: The sketch of the built-in electric potential (blue line) of the junction $U(z)$. The crossing points z_i correspond to locations where the electron-like (green line) and hole-like (orange line) Weyl nodes cross the Fermi level.

junctions [124] the probability of Klein tunneling in valley i is determined by the value of the built-in electric field E_i at the crossing points, z_i, where the electrochemical potential crosses the Weyl node, i.e. $U(z_i) + \Delta_i = 0$, see Fig. 5.1. Therefore we start by expressing the conductance in terms of the electric fields E_i at the crossing points and then evaluate these fields by solving the corresponding nonlinear screening problem.

5.2 *Conductance of a Weyl Semimetal p-n Junction*

5.2.1 Conductance at zero magnetic field

Let us consider transmission of an electron at the Fermi level across the junction. For an electron in valley i with momentum parallel to the junction plane, $\hbar\mathbf{k}_\| = \hbar(k_x, k_y)$, the transmission coefficient may be determined by solving an one-dimensional Dirac equation,

$$\begin{pmatrix} -i\hbar v\,\partial_z + U(z) + \Delta_i & v\hbar k_\| \\ v\hbar k_\|^* & i\hbar v\,\partial_z + U(z) + \Delta_i \end{pmatrix} \begin{pmatrix} u \\ v \end{pmatrix} = 0. \tag{5.2}$$

Here the complex wavenumber $k_\| = k_x - ik_y$ parameterizes the conserved momentum parallel to the junction plane. We will assume that the dimensionless coupling constant $\alpha = ge^2/\hbar v$ is small. In this case, in the region relevant for Klein tunneling, which is of order $l_{E_i} = \sqrt{\hbar v/|e|E_i}$ near the crossing points, the potential can be approximated by $U(z) + \Delta_i = -eE_i(z - z_i)$. In such case the transmission coefficient is well known

$$\mathcal{T}_i(|k_\||) = \exp\left(-\pi|k_\||^2 l_{E_i}^2\right). \tag{5.3}$$

This result may be understood from a semiclassical consideration. For a given $k_\|$ the value of the z-component of the electron momentum is dictated by energy conservation, $vp_z(z) = \pm\sqrt{\left[eE_i(z - z_i)\right]^2 - (\hbar v|k_\||)^2}$, which yields the stopping points $z_i \pm |k_\||l_{E_i}$. The transmission coefficient is determined by the imaginary part of the action of the tunneling trajectory accumulated in the classically forbidden region between the stopping points, $\mathcal{T}_i(|k_\||) = \exp\left(-2\,\mathrm{Im}\int p_z(z)dz/\hbar\right) = \exp\left(-\pi|k_\||^2 l_{E_i}^2\right)$. This coincides with the exact result, Eq. (5.3), according to which only electrons with small parallel momenta, $|k_\|| \le l_{E_i}^{-1}$, have an appreciable transmission probability.

Substituting Eq. (5.3) into the Landauer formula and summing over valleys and $k_\|$, we obtain the conductance of the junction

$$G = \frac{e^2}{h}\sum_i \frac{S}{(2\pi l_{E_i})^2}, \tag{5.4}$$

where S is the area of the junction.

5.2.2 Magnetoconductance

Next we consider the magnetic field dependence of the junction conductance $G(B)$ at zero temperature for a magnetic field perpendicular to the plane of the junction. In the vicinity of the crossing points the electron Hamiltonian has the form $H_i = v\,\boldsymbol{\sigma}\cdot\left(-i\hbar\boldsymbol{\nabla} - \frac{e}{c}\mathbf{A}\right) - eE_i z$. Using the Landau gauge for the vector potential, $\mathbf{A} = (0, Bx, 0)$, we look for the energy eigenstates in the form $\psi^T = e^{ik_y y}(u(x,z), v(x,z))$. The spinor amplitudes u and v satisfy the Dirac equation

$$\hbar v \begin{pmatrix} \frac{\partial}{\partial z} - i\frac{z}{l_{E_i}^2} & \frac{\partial}{\partial x} - \frac{x-x_0}{l_B^2} \\ \frac{\partial}{\partial x} + \frac{x-x_0}{l_B^2} & -\frac{\partial}{\partial z} - i\frac{z}{l_{E_i}^2} \end{pmatrix} \begin{pmatrix} u \\ v \end{pmatrix} = 0, \tag{5.5}$$

with $l_B = \sqrt{\hbar c/|e|B}$ being the magnetic length and $x_0 = k_y l_B^2$. The solutions have the form $(u, v) = (\phi_{n-1}(x)\tilde{u}_{n-1}(z), \phi_n(x)\tilde{v}_n(z))$, where $\phi_n(x)$ are wavefunctions of the n-th Landau level. The amplitudes $\tilde{u}$ and $\tilde{v}$ obey the differential equation

$$\hbar v \begin{pmatrix} \frac{\partial}{\partial z} - i\frac{z}{l_{E_i}^2} & \frac{\sqrt{2n}}{l_B} \\ \frac{\sqrt{2n}}{l_B} & -\frac{\partial}{\partial z} - i\frac{z}{l_{E_i}^2} \end{pmatrix} \begin{pmatrix} \tilde{u}_{n-1}(z) \\ \tilde{v}_n(z) \end{pmatrix} = 0. \tag{5.6}$$

Note that in addition to "conventional" Landau levels there is one chiral, $n = 0$, Landau level (in this case $\tilde{u}_{n-1} = 0$). Since Eq. (5.6) coincides with Eq. (5.2) for a quantized value of the parallel momentum, $|k_{\parallel,n}| = \sqrt{2n}/l_B$, the transmission coefficient for the n-th Landau level may be obtained by substituting $|k_{\parallel,n}| = \sqrt{2n}/l_B$ in Eq. (5.3).

$$\mathcal{T}_{n,i} = \exp\left(-2\pi n\,\frac{l_{E_i}^2}{l_B^2}\right). \tag{5.7}$$

Substituting Eq. (5.7) into the Landauer formula, summing over the Landau levels and accounting for their degeneracy, $S/(2\pi l_B^2)$, we get the magnetic field dependence of the conductance

$$G(B) = \frac{e^2}{h}\frac{S}{2\pi l_B^2}\sum_i \frac{1}{1 - e^{-2\pi l_{E_i}^2/l_B^2}}\,, \tag{5.8}$$

which is plotted in Fig. 5.2 ($\theta = 0$ curve). As expected, at $B \to 0$ the above expression reproduces the zero field result, Eq. (5.4).

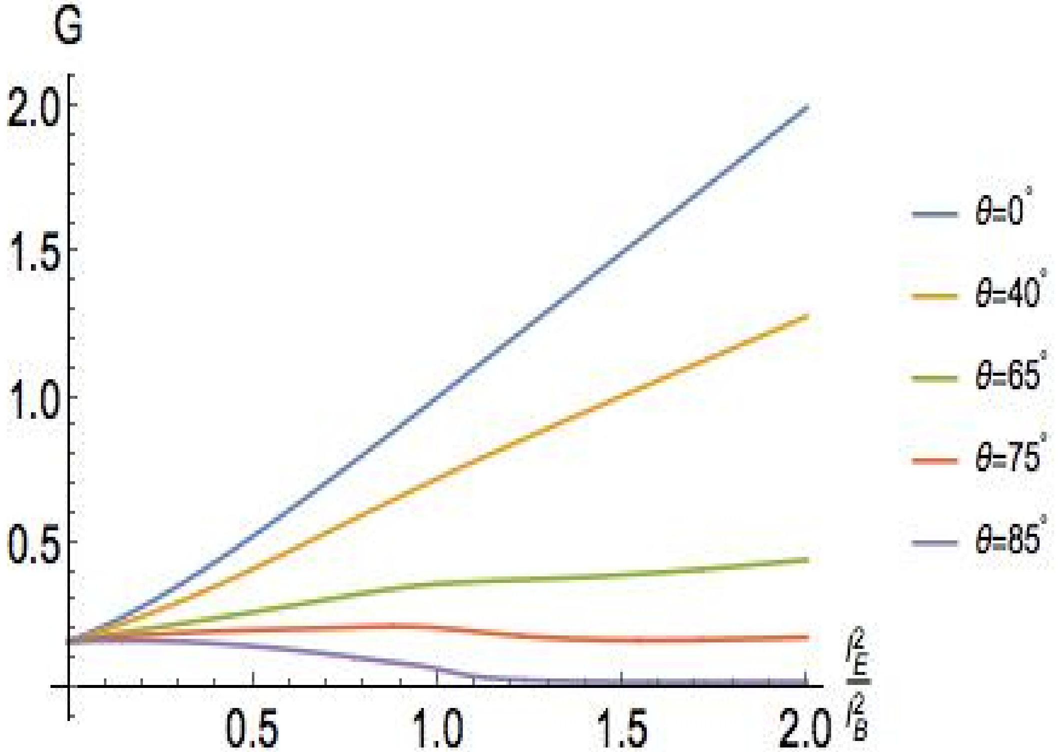

Figure 5.2: The magnetic field dependence of the conductance G at different angles θ between the magnetic field and the normal to the junction plane. G is measured in the units of the $\frac{e^2}{h}\frac{S}{2\pi l_E^2}$.

It follows from Eq. (5.8) that $G(B)$ is a monotonically increasing function of the magnetic field. Note that the magnetoconductance is a linear function of the magnetic field, $\delta G(B) = G(B) - G(0) \sim B$, at both weak ($l_B \gg l_E$) and strong ($l_E \gg l_B$) fields. The positive magnetoconductance (or negative MR) is a signature of the chiral anomaly in Weyl materials [98, 110, 111, 139]. At strong fields, $l_B \ll l_E$, the conductance is determined entirely by the electrons in the chiral ($n = 0$) Landau levels, which move between the p- and n- regions without backscattering. In this case the positive magnetoconductance is due to the linear in B growth of Landau level degeneracy.

The results (5.4) and (5.8) assume absence of scattering and inter-valley electric or magnetic breakdown. They hold provided the electron mean free path exceeds l_E and l_B, and the magnetic field and the built-in electric field are not too strong; $\Delta K \gg l_E^{-1}, l_B^{-1}$ (here ΔK is the momentum difference between the Weyl nodes). The electric fields E_i must be determined by solving a nonlinear screening problem inside the junction.

5.2.3 Tilted magnetic field.

In the most general situation, in which the magnetic field makes an angle θ with the normal to the junction plane, the electron transmission problem can be solved analytically. The resulting conductance of the junction is obtained in the supplementary materials [**?**] and is given by,

$$G(B) = \frac{e^2}{h} \frac{S\cos\theta}{2\pi l_B^2} \sum_i \frac{\cos\alpha_i(\theta)}{1 - \exp(-2\pi\sqrt{\frac{|\lambda_{i-}|}{\lambda_{i+}}})}, \tag{5.9}$$

where

$$\lambda_{i\pm} = \frac{1}{2}\sqrt{\left(\frac{l_B^4}{l_{Ei}^4} - 1\right)^2 + \frac{4\cos^2\theta\, l_B^4}{l_{Ei}^4}} \pm \frac{1}{2}\left(\frac{l_B^4}{l_{Ei}^4} - 1\right),$$

$$\tan 2\alpha_i(\theta) = \frac{\sin 2\theta}{\cos 2\theta + l_B^4/l_{Ei}^4}.$$

For $\theta = 0$ this expression reproduces Eq. (5.8). Magnetoconductance remains positive and linear in B at both low and high fields for most tilting angles θ, see Fig. 5.2. For $\theta \geq 70^\circ$ magnetoconductance becomes non-monotonic and develops a shoulder-like feature at

$l_B/l_E \sim 1$. The latter arises because at $l_B/l_E \gg 1$ Klein tunneling occurs along the z-axis, whereas at $l_B/l_E \ll 1$ tunneling occurs in the direction of the magnetic field. As a result, for θ close to 90° the apparent area of the junction, available for tunneling sharply decreases as the increasing magnetic field passes $l_B = l_E$.

5.3 Evaluation of the built-in electric field

For simplicity, below we assume that the offsets in the electron-like and hole-like valleys are equal in magnitude, $\Delta_i = \pm\Delta$. The corresponding density of states has the form $\nu(\varepsilon) = g(\varepsilon^2+\Delta^2)/\pi^2\hbar^3v^3$, and the number density of electrons depends on the electrostatic potential as $n(U) = -g\left(U^3 + 3\Delta^2 U\right)/(3\pi^2\hbar^3v^3)$. The electrostatic potential $U(z)$ obeys the following Poisson equation,

$$\frac{d^2U(z)}{dz^2} = 4\pi e^2\left[-n_\mathrm{d}(z) + g\frac{U^3+3\Delta^2 U}{3\pi^2\hbar^3v^3}\right], \tag{5.10}$$

where $n_\mathrm{d}(z)$ is the dopant density, which we model as $n_\mathrm{d}(z) = n_0\,\mathrm{sgn}(z)\Theta(|z|-d)$ with $\Theta(x)$ being the step function.

Before presenting an analytic solution of Eq. (5.10) let us begin with a qualitative discussion of its essential features. Deep inside the doping regions, $|z| \gg d$, the electrostatic potential approaches constant values $\pm\varepsilon_F$ determined by the dopant density n_0. In the middle of the junction $|U(z)| \ll \Delta$, and the screening is linear, with the intrinsic screening length $\kappa^{-1} = \sqrt{\pi/4\alpha}\,\hbar v/\Delta$. At $|U(z)| \geq \Delta$ screening becomes nonlinear. Since the creation of the p-n junction requires $|U(z)| > \Delta$ one should distinguish between the following two cases: *i*) moderate doping, $\varepsilon_F \geq \Delta$, and *ii*) strong doping, $\varepsilon_F \gg \Delta$. In either case we assume that the junction width d exceeds the screening length in the doping region, $d \gg (\sqrt{\alpha}\,\varepsilon_F/\hbar v)^{-1}$. The magnitude E_* of the electric field at the crossing points in these regimes may be estimated as follows.

i) For moderate doping, $\varepsilon_F \geq \Delta$, the crossing points are located within the screening length κ^{-1} from the boundary of the doping regions, and the electric field at the crossing points may be estimated as $E_* \sim \varepsilon_F\kappa/|e|$. Here we assume that Fermi energies in different valleys are of the same order ε_F. Using Eq. (5.4) the conductance can be estimated as

$$G(0) \approx \frac{e^2}{2\pi h} \frac{gS}{2\pi} k_F \kappa, \quad k_F = \frac{\varepsilon_F}{\hbar v}. \tag{5.11}$$

Note that the conductance turns out to be independent of the junction width d.

ii) For strong doping, $\varepsilon_F \gg \Delta$, near the boundary with the doping region, $d - |z| \ll \kappa^{-1}, d$, the last term in Eq. (5.10) may be neglected and the solution (on the doping-free side) acquires a simple form,

$$U(z) \approx A/(d + z_0 - |z|).$$

Since inside the doping region $|U(z)| \sim \varepsilon_F$ and the screening length is $\sim (k_F \sqrt{\alpha})^{-1}$ continuity of the potential and electric field at $|z| = d$ yields $|A| \sim v/\sqrt{\alpha}$, and $z_0 \sim 1/(\sqrt{\alpha} k_F)$. Thus the locations of the crossing points, $|U(z_*)| = \Delta$, may be estimated as $d - |z_*| \sim \min\{\kappa^{-1}, d\}$, and the electric field in them as, $E_* \sim \hbar v / |e| \sqrt{\alpha} \min\{\kappa^{-2}, d^2\}$. This results the following estimate for the junction conductance,

$$G \sim \frac{e^2}{2\pi h} \frac{gS}{\sqrt{\alpha} \min\{\kappa^{-2}, d^2\}}.$$

Note that at strong doping the conductance becomes independent of the doping level ε_F.

Let us now turn to the quantitative treatment of the nonlinear screening problem. The first integral of the Poisson equation (5.10) can be cast in the following dimensionless form,

$$\tilde{U}_\zeta^2 = \left(\tilde{U} - 1\right)^2 \left(\tilde{U}^2 + 2\tilde{U} + 3 + 6\delta^2\right), \zeta > \zeta_d, \tag{5.12a}$$

$$\tilde{U}_\zeta^2 = \tilde{U}^4 + 6\delta^2 \tilde{U}^2 + \tilde{E}_c^2, \; 0 < \zeta < \zeta_d, \tag{5.12b}$$

where $\tilde{U} = U/\varepsilon_F$, $\delta = \Delta/\varepsilon_F$, $\zeta = \sqrt{2\alpha/3\pi} k_F z$ and $\tilde{E}_c = \sqrt{3\pi/2\alpha}\, |e| E_c/(k_F \varepsilon_F)$ are, respectively, the dimensionless electrostatic potential, energy offset, coordinate, and electric field at the center of the junction. Finally, $\tilde{U}_\zeta$ denotes the first derivative of $\tilde{U}$ with respect to ζ and ϵ_F is related to the dopant density by $n_0 = 4\alpha(1 + 3\delta^2)\, k_F \varepsilon_F^2 / (3\pi^2 e^2)$.

The solution of Eqs. (5.12a) inside the doping region $\zeta > \zeta_d$ is given by

$$\tilde{U} = 1 - \frac{3\sqrt{2}\,(1 + \delta^2)}{\sqrt{2} + \sqrt{1 + 3\delta^2} \sinh \sqrt{6(1 + \delta^2)}(\zeta - \zeta_0)}. \tag{5.13}$$

The solution of Eq. (5.12b) in the doping-free region is given by

$$\tilde{U} = -ia_- \, sn\left(ia_+\zeta, k\right), \tag{5.14}$$

where $sn(u,k)$ is the Jacobi elliptic function [140], and the parameters $a_\pm$ and k are given by

$$a_\pm = \sqrt{3\delta^2 \pm \sqrt{9\delta^4 - \tilde{E}_c^2}}, \quad k = \frac{a_-}{a_+}. \tag{5.15}$$

The integration constants ζ_0 and $\tilde{E}_c$ in Eqs. (5.13) and (5.14) are determined from the following equations, which express the continuity of the potential $\tilde{U}$ and its derivative at the boundary of the doping region ($\zeta = \zeta_d$),

$$\begin{aligned} \frac{3\sqrt{2}\,(1+\delta^2)}{\sqrt{2}+\sqrt{1+3\delta^2}\sinh\left[\sqrt{6(1+\delta^2)}(\zeta_d-\zeta_0)\right]} - 1 &= ia_- s_d, \\ \frac{6\sqrt{3}\,(1+\delta^2)\cosh\left[\sqrt{6(1+\delta^2)}(\zeta_d-\zeta_0)\right]}{\left\{\sqrt{2}+\sqrt{1+3\delta^2}\sinh\left[\sqrt{6(1+\delta^2)}(\zeta_d-\zeta_0)\right]\right\}^2} &= \tilde{E}_c c_d d_d. \end{aligned}$$

Here the abbreviations s_d, c_d and d_d stand for

$$s_d \equiv sn(ia_+\zeta_d, k),\; c_d \equiv cn(ia_+\zeta_d, k),\; d_d \equiv dn(ia_+\zeta_d, k).$$

The dimensionless electric field at the center of the junction, $\tilde{E}_c$ can be found by solving the above equations numerically. For the dimensionless electric field $\tilde{E}_*$ at the crossing points, $\tilde{U}(\zeta_*) = \pm\delta$, using Eq. (5.12b) we get

$$\tilde{E}_*^2 = \tilde{E}_c^2 + 7\delta^4. \tag{5.17}$$

At strong doping determination of the potential inside the undoped region can be further simplified. In this case both $\tilde{E}_c$ and δ are small, and by Eq. (5.15) so are $a_\pm$. Then the matching conditions can be satisfied only if the function $sn(ia_+\zeta, k)$ in Eq. (5.14) has a pole near the boundary with the doping region, $\zeta \approx \zeta_d$. Since in real space the location of the pole is offset from $\pm d$ by a distance of order of the screening length in the doping region, then to accuracy $1/(\sqrt{\alpha}k_F d)$ we can determine $\tilde{E}_c$ from the condition that $sn(ia_+\zeta, k)$ in Eq. (5.14) must have a pole at $\zeta = \zeta_d$.

The Jacobi elliptic function $sn(w, k)$ has a series of simple poles at $w = w_{mn} = 2mK(k) + (2n+1)iK(\sqrt{1-k^2})$ with residues $(-1)^m/k$. Here m, n are integers, and

$$K(k) = \int_0^{\pi/2} d\phi/\sqrt{1-k^2\sin^2\phi},$$

is the complete elliptic integral of the first kind. Near the poles the dimensionless potential $\tilde{U}$ in Eq. (5.14) has the form, $\tilde{U}(\zeta) \approx (-1)^{m+1}/(\zeta + i\zeta_{mn}/a_+)$. Since $\tilde{U}$ must be real for real ζ the pole at $\zeta = \zeta_d$ corresponds to $m = n = 0$. This gives the condition that determines the dimensionless electric field $\tilde{E}_c$ at the center of the junction,

$$\zeta_d = \frac{1}{a_+} K\left(\sqrt{1-k^2}\right). \tag{5.18}$$

The right hand side of this condition is real for all values of $\tilde{E}_c$. For $\tilde{E}_c < 3\delta^2$ this is obvious since in this regime $0 < k < 1$ and a_+ is real, see Eq. (5.15). For $\tilde{E}_c > 3\delta^2$ the location of the pole remains real although the parameters $a_\pm$ and k become complex. To see this we express $\tilde{E}_c$ in terms of a parameter θ in the form

$$\tilde{E}_c = \frac{3\delta^2}{\cosh\theta}. \tag{5.19}$$

Here θ is real and positive for $\tilde{E}_c < 3\delta^2$, and becomes purely imaginary, $\theta \to i\vartheta, 0 < \vartheta < \pi/2$, for $3\delta^2 < \tilde{E}_c$. The parameters $a_\pm$, and k in Eq. (5.15) may be expressed in terms of θ as $a_\pm = \frac{\sqrt{3}\, e^{\pm\theta/2}}{\sqrt{\cosh\theta}}\,\delta$, and $k = e^{-\theta}$. Using the identity $K(\sqrt{1-k^2}) = \frac{2}{1+k} K\left(\frac{1-k}{1+k}\right)$, see formula 13.8 (12) of Ref. [140], we can rewrite Eq. (5.18) in the form

$$\delta\,\zeta_d = \frac{\sqrt{\cosh(\theta)/3}}{\cosh(\theta/2)} K\left(\tanh\left(\frac{\theta}{2}\right)\right), \tag{5.20}$$

that is explicitly real for all values of the electric field $\tilde{E}_c$. The electric field $\tilde{E}_*$ at the crossing points may be obtained using Eqs. (5.17) and (5.19).

In the limiting case of $d \gg 1/\kappa$ (strong intrinsic screening) $\tilde{E}_c \ll 3\delta^2$ we have $\theta \gg 1$ and Eq. (5.20) simplifies to $\tilde{E}_c \approx 24\delta^2 e^{-\sqrt{6}\delta\zeta_d} = 24\delta^2 e^{-\kappa d}$. The characteristic length l_{E_*} at the crossing points can be found from Eq. (5.17)

$$l_{E_*}^{-2} \approx \sqrt{\frac{7\pi}{24\alpha}}\kappa^2 \approx \frac{0.96}{\sqrt{\alpha}}\kappa^2. \tag{5.21}$$

In the opposite limit of $d \ll 1/\kappa$ (weak intrinsic screening) we have $\theta = i\vartheta \to i\pi/2$, and Eq. (5.20) yields $\tilde{E}_c \approx 2K^2(-i)/\zeta_d^2 = 3\pi K^2(-i)/\alpha d^2$. The characteristic length l_{E_*} corresponding to the electric field at the crossing points is given by

$$l_{E_*}^{-2} \approx \sqrt{\frac{6\pi}{\alpha}}K^2(-i)\frac{1}{d^2} \approx \frac{7.45}{\sqrt{\alpha}\,d^2}. \tag{5.22}$$

The junction conductance (5.4) in these limiting cases is expressed in the form,

$$G(0) \approx \frac{e^2}{2\pi h}\frac{g\,S}{2\pi\sqrt{\alpha}}\begin{cases} 0.96\kappa^2, & d \gg \kappa^{-1}, \\ 7.45 d^{-2}, & d \ll \kappa^{-1}. \end{cases}$$

As expected, at strong doping it is independent of the doping level ε_F.

We note that the assumption that the potential $U(z)$ changes linearly with z in the interval of order l_E near the crossing points is justified as long as the dimensionless coupling constant is small, $\alpha \ll 1$.

It is important to note that the MR of the junction can be significant even in the interval of magnetic fields where it can be treated semiclassically in the regions of the junction. Therefore one can neglect the magnetic field dependence of the density of states in these regions. Finally we note that the value of E_c is unaffected by the magnetic field in all cases considered above.

We would like to discuss differences between the above negative MR in p-n junctions and recently observed negative MR of bulk Weyl semimetals. In bulk Weyl semimetals at $\varepsilon_F \gg \hbar v/l_B$ electrons can be described semiclassically. In the latter case the magnitude of the negative MR is quadratic in B [98, 139]. It exists only in a situation where the inter-valley relaxation time is much longer than the intra-valley one and only in certain interval of angles between the external electric and magnetic fields, and only in some (usually small) interval of angles between the external electric and magnetic fields. In contrast, the negative

MR of p-n junction is governed by the parameter l_E/l_B and is independent of the relaxation times. Both at small and large magnetic fields its magnitude is linear in B.

Another way to distinguish the contribution of p-n junction to the total negative MR of the device is to study it as a function of the bias voltage V on the junction: the value of $G(V, B)$ should exhibit characteristic asymmetry with respect to a change $V \to -V$ for diodes.

BIBLIOGRAPHY

[1] N. W. Ashcroft and N. D. Mermin. *Solid State Physics.* (Holt, Rinehart and Winston), New York; London, 1977.

[2] A. A. Abrikosov. *Fundamentals of the Theory of Metals.* (North-Holland), 1988.

[3] D. Xiao, M.-C. Chang, and Q. Niu. Berry phase effects on electronic properties. *Rev. Mod. Phys.*, **82**:1959–2007, Jul 2010.

[4] M.-C. Chang and Q. Niu. Berry phase, hyperorbits, and the hofstadter spectrum: Semiclassical dynamics in magnetic bloch bands. *Phys. Rev. B*, **53**:7010–7023, Mar 1996.

[5] G. Sundaram and Q. Niu. Wave-packet dynamics in slowly perturbed crystals: Gradient corrections and berry-phase effects. *Phys. Rev. B*, **59**:14915–14925, Jun 1999.

[6] A. Bohm, A. Mostafazadeh, H. Koizumi, Q. Niu, and J. Zwanziger. *The Geometric Phase in Quantum Systems Foundations, Mathematical Concepts, and Applications in Molecular and Condensed Matter Physics.* (Springer Berlin Heidelberg), 2003.

[7] F. D. M. Haldane. Berry curvature on the fermi surface: Anomalous hall effect as a topological fermi-liquid property. *Phys. Rev. Lett.*, **93**:206602, Nov 2004.

[8] R. Karplus and J. M. Luttinger. Hall effect in ferromagnetics. *Phys. Rev.*, **95**:1154–1160, Sep 1954.

[9] N. Nagaosa, J. Sinova, S. Onoda, A. H. MacDonald, and N. P. Ong. Anomalous hall effect. *Rev. Mod. Phys.*, **82**:1539–1592, May 2010.

[10] J. Smit. The spontaneous hall effect in ferromagnetics i. *Physica*, **21**(6):877 – 887, 1955.

[11] J. Smit. The spontaneous hall effect in ferromagnetics ii. *Physica*, **24**(1):39 – 51, 1958.

[12] L. Berger. Side-jump mechanism for the hall effect of ferromagnets. *Phys. Rev. B*, **2**:4559–4566, Dec 1970.

[13] V. I. Belinicher, E. L. Ivchenko, and B. I. Sturman. Kinetic theory of the displacement photovoltaic effect in piezoelectrics. *Sov. Phys. JETP*, **56**:359, 1982.

[14] N. A. Sinitsyn. Semiclassical theories of the anomalous hall effect. *Journal of Physics: Condensed Matter*, **20**(2):023201, 2008.

[15] A. P. Mackenzie and Y. Maeno. The superconductivity of Sr_2RuO_4 and the physics of spin-triplet pairing. *Rev. Mod. Phys.*, **75**:657–712, May 2003.

[16] K. D. Nelson, Z. Q. Mao, Y. Maeno, and Y. Liu. Odd-parity superconductivity in Sr_2RuO_4. *Science*, **306**(5699):1151–1154, 2004.

[17] F. Kidwingira, J. D. Strand, D. J. Van Harlingen, and Y. Maeno. Dynamical superconducting order parameter domains in Sr_2RuO_4. *Science*, **314**(5803):1267–1271, 2006.

[18] J. Xia, Y. Maeno, P. T. Beyersdorf, M. M. Fejer, and A. Kapitulnik. High resolution polar kerr effect measurements of Sr_2RuO_4: Evidence for broken time-reversal symmetry in the superconducting state. *Phys. Rev. Lett.*, **97**:167002, Oct 2006.

[19] G. M. Luke, Y. Fudamoto, K. M. Kojima, M. I. Larkin, J. Merrin, B. Nachumi, Y. J. Uemura, Y. Maeno, Z. Q. Mao, Y. Mori, H. Nakamura, and M. Sigrist. Time-reversal symmetry-breaking superconductivity in Sr_2RuO_4. *Nature*, **394**(6693):558–561, 08 1998.

[20] Y. Maeno, S. Kittaka, T. Nomura, S. Yonezawa, and K. Ishida. Evaluation of spin-triplet superconductivity in Sr_2RuO_4. *Journal of the Physical Society of Japan*, **81**(1):011009, 2012.

[21] T. M. Rice and M. Sigrist. Sr_2RuO_4 : an electronic analogue of 3-He? *Journal of Physics: Condensed Matter*, **7**(47):L643, 1995.

[22] S. NishiZaki, Y. Maeno, and Z. Q. Mao. Effect of impurities on the specific heat of the spin-triplet superconductor Sr_2RuO_4. *Journal of Low Temperature Physics*, **117**(5):1581–1585, 1999.

[23] K. Ishida, H. Mukuda, Y. Kitaoka, Z. Q. Mao, Y. Mori, and Y. Maeno. Anisotropic superconducting gap in the spin-triplet superconductor Sr_2RuO_4: Evidence from a Ru-NQR study. *Phys. Rev. Lett.*, **84**:5387–5390, Jun 2000.

[24] P. G. Björnsson, Y. Maeno, M. E. Huber, and K. A. Moler. Scanning magnetic imaging of Sr_2RuO_4. *Phys. Rev. B*, **72**:012504, Jul 2005.

[25] J. R. Kirtley, C. Kallin, C. W. Hicks, E.-A. Kim, Y. Liu, K. A. Moler, Y. Maeno, and K. D. Nelson. Upper limit on spontaneous supercurrents in Sr_2RuO_4. *Phys. Rev. B*, **76**:014526, Jul 2007.

[26] C. W. Hicks, J. R. Kirtley, T. M. Lippman, N. C. Koshnick, M. E. Huber, Y. Maeno, W. M. Yuhasz, M. B. Maple, and K. A. Moler. Limits on superconductivity-related magnetization in Sr_2RuO_4 and $PrOs_4Sb_{12}$ from scanning squid microscopy. *Phys. Rev. B*, **81**:214501, Jun 2010.

[27] Z. Q. Mao, Y. Maeno, S. NishiZaki, T. Akima, and T. Ishiguro. In-plane anisotropy of upper critical field in Sr_2RuO_4. *Phys. Rev. Lett.*, **84**:991–994, Jan 2000.

[28] A. G. Aronov, Yu. M. Gal'perin, V. L. Gurevich, and V. I. Kozub. The boltzmann-equation description of transport in superconductors. *Advances in Physics*, **30**(4):539–592, 1981.

[29] D. N. Langenberg and A. I. Larkin. *Nonequilibrium Superconductivity, Chapter 8.* Elsevier, 1986.

[30] L. D. Landau and E. M. Lifshitz. *Quantum Mechanics : Non-relativistic Theory.* (Butterworth-Heinemann), Amsterdam, 2004.

[31] R. M. White and T. H. Geballe. *Long Range Order in Solids.* (Academic Press), New York, 1979.

[32] R. M. Lutchyn, P. Nagornykh, and V. M. Yakovenko. Frequency and temperature dependence of the anomalous ac hall conductivity in a chiral $p_x + ip_y$ superconductor with impurities. *Phys. Rev. B*, **80**:104508, Sep 2009.

[33] E. Taylor and C. Kallin. Intrinsic hall effect in a multiband chiral superconductor in the absence of an external magnetic field. *Phys. Rev. Lett.*, **108**:157001, Apr 2012.

[34] Catherine Kallin. Chiral p-wave order in Sr_2RuO_4. *Reports on Progress in Physics*, **75**(4):042501, 2012.

[35] A. Keles, A. V. Andreev, and B. Z. Spivak. Electron transport in p-wave superconductor-normal metal junctions. *Phys. Rev. B*, **89**:014505, Jan 2014.

[36] J. A. Sauls. The order parameter for the superconducting phases of UPt_3. *Advances in Physics*, **43**(1):113–141, 1994.

[37] J. D. Strand, D. J. Bahr, D. J. Van Harlingen, J. P. Davis, W. J. Gannon, and W. P. Halperin. The transition between real and complex superconducting order parameter phases in UPt_3. *Science*, **328**(5984):1368–1369, 2010.

[38] J. D. Strand, D. J. Van Harlingen, J. B. Kycia, and W. P. Halperin. Evidence for complex superconducting order parameter symmetry in the low-temperature phase of UPt_3 from josephson interferometry. *Phys. Rev. Lett.*, **103**:197002, Nov 2009.

[39] E. R. Schemm, R. E. Baumbach, P. H. Tobash, F. Ronning, E. D. Bauer, and A. Kapitulnik. Evidence for broken time-reversal symmetry in the superconducting phase of URu_2Si_2. *Phys. Rev. B*, **91**:140506, Apr 2015.

[40] E. R. Schemm, W. J. Gannon, C. M. Wishne, W. P. Halperin, and A. Kapitulnik. Observation of broken time-reversal symmetry in the heavy-fermion superconductor UPt_3. *Science*, **345**(6193):190–193, 2014.

[41] Andre K. Geim. Nobel lecture: Random walk to graphene. *Rev. Mod. Phys.*, **83**:851–862, Aug 2011.

[42] K. S. Novoselov, D. Jiang, F. Schedin, T. J. Booth, V. V. Khotkevich, S. V. Morozov, and A. K. Geim. Two-dimensional atomic crystals. *Proceedings of the National Academy of Sciences of the United States of America*, **102**(30):10451–10453, 2005.

[43] A. K. Geim and I. V. Grigorieva. Van der waals heterostructures. *Nature*, **499**(7459):419–425, 07 2013.

[44] K. F. Mak, C. Lee, J. Hone, J. Shan, and T. F. Heinz. Atomically thin MoS_2: A new direct-gap semiconductor. *Phys. Rev. Lett.*, **105**:136805, Sep 2010.

[45] D. Xiao, W. Yao, and Q. Niu. Valley-contrasting physics in graphene: Magnetic moment and topological transport. *Phys. Rev. Lett.*, **99**:236809, Dec 2007.

[46] D. Xiao, G.-B. Liu, W. Feng, X. Xu, and W. Yao. Coupled spin and valley physics in monolayers of MoS_2 and other group-VI dichalcogenides. *Phys. Rev. Lett.*, **108**:196802, May 2012.

[47] X. Xu, W. Yao, D. Xiao, and T. F. Heinz. Spin and pseudospins in layered transition metal dichalcogenides. *Nat. Phys*, **10**(5):343–350, 05 2014.

[48] C.-H. Lee, G.-H. Lee, A. M. van der Zande, W. Chen, Y. Li, M. Han, X. Cui, G. Arefe, C. Nuckolls, T. F. Heinz, J. Guo, J. Hone, and P. Kim. Atomically thin *p*-*n* junctions with van der waals heterointerfaces. *Nat. Nano*, **9**(9):676–681, 09 2014.

[49] V. I. Belinicher and B. I. Sturman. The photogalvanic effect in media lacking a center of symmetry. *Soviet Physics Uspekhi*, **23**(3):199, 1980.

[50] E. L. Ivchenko. *Optical spectroscopy of semiconductor nanostructures.* Alpha Science International, Pangbourne, England, 2004.

[51] H. Yuan, X. Wang, B. Lian, H. Zhang, X. Fang, B. Shen, G. Xu, Y. Xu, S.-C. Zhang, H. Y. Hwang, and Y. Cui. Generation and electric control of spin–valley-coupled circular photogalvanic current in WSe_2. *Nat. Nano*, **9**(10):851–857, 10 2014.

[52] E. L. Ivchenko and G. E. Pikus. New photogalvanic effect in gyrotropic crystals. *JETP Lett.*, **27**:604, 1978.

[53] V. I. Belinicher. Space-oscillating photocurrent in crystals without symmetry center. *Physics Letters A*, 66(3):213 – 214, 1978.

[54] E. L. Ivchenko, Y. B. Lyanda-Geller, G. E. Pikus, and R. Ya. Rasulov. *Sov. Phys. Semicond.*, **18**:55, 1984.

[55] V. I. Belinicher. *Sov. Phys. Solid State.*, **24**:450, 1982.

[56] N. S. Averkiev and M. I. Dyakonov. Resonance structure in the magnetic-field dependence of the kinetic coefficients of a paramagnetic gas. *JETP Lett.*, **35**:241, 1982.

[57] Y. B. Lyanda-Geller. Displacement current of polarized carriers. *JETP Lett.*, **46**:489, 1987.

[58] E. L. Ivchenko, Yu. B. Lyanda-Geller, and G. E. Pikus. Circular magnetophotocurrent and spin splitting of band states in optically-inactive crystals. *Solid State Communications*, 69(6):663 – 665, 1989.

[59] E. L. Ivchenko, Y. B. Lyanda-Geller, and G. E. Pikus. Photocurrent in structures with quantum wells with an optical orientation of free carriers. *JETP Lett.*, **50**:175, 1989.

[60] E. L. Ivchenko, Y. B. Lyanda-Geller, and G. E. Pikus. Current of thermalized spin-oriented photocarriers. *Sov. Phys. JETP*, **71**:550, 1990.

[61] V. M. Asnin, A. A. Bakun, A. M. Danishevskii, E. L. Ivchenko, G. E. Pikus, and A. A. Rogachev. Observation of a photo-emf that depends on the sign of the circular polarization of the light. *JETP Lett.*, **28**:74, 1978.

[62] A. V. Andrianov and I. D. Yaroshetskii. Magnetic-field-induced circular photovoltaic effect in semiconductors. *JETP Lett.*, **40**:882, 1984.

[63] A. A. Bakun, B. P. Zakharchenya, A. A. Rogachev, M. N. Tkachuk, and V. G. Fleisher. Observation of a surface photocurrent caused by optical orientation of electrons in a semiconductor. *JETP Lett.*, **40**:1293, 1984.

[64] A. V. Andrianov, E. V. Beregulin, Y. B. Lyanda-Geller, and I. D. Yaroshetskii. Magnetic-field-induced photovoltaic effect in p-type gallium arsenide. *Sov. Phys. JETP*, **75**:921, 1992.

[65] S. D. Ganichev, E. L. Ivchenko, S. N. Danilov, J. Eroms, W. Wegscheider, D. Weiss, and W. Prettl. Conversion of spin into directed electric current in quantum wells. *Phys. Rev. Lett.*, **86**:4358–4361, May 2001.

[66] R. Raimondi, P. Schwab, C. Gorini, and G. Vignale. Spin-orbit interaction in a two-dimensional electron gas: A $SU(2)$ formulation. *Annalen der Physik*, **524**(3-4):153–162, 2012.

[67] I. L. Aleiner and Y. B. Lyanda-Geller. (unpublished).

[68] J. M. Luttinger. Theory of the hall effect in ferromagnetic substances. *Phys. Rev.*, **112**:739–751, Nov 1958.

[69] E. V. Beregulin, S. D. Ganichev, K. Y. Glukh, Y. B. Lyanda-Geller, and I. D. Yaroshetskii. *Sov. Phys. Solid State*, **31**:63, 1989.

[70] S. A. Tarasenko. Direct current driven by ac electric field in quantum wells. *Phys. Rev. B*, **83**:035313, Jan 2011.

[71] B. Radisavljevic, A. Radenovic, J. Brivio, V. Giacometti, and A. Kis. Single-layer MoS_2 transistors. *Nat. Nano*, **6**(3):147–150, 03 2011.

[72] A. Kormanyos, G. Burkard, M. Gmitra, J. Fabian, V. Zlyomi, N. D. Drummond, and V. I. Falko. *2D Materials*, **2**(2):022001, 2015.

[73] M. Shinada and S. Sugano. Interband optical transitions in extremely anisotropic semiconductors. i. bound and unbound exciton absorption. *Journal of the Physical Society of Japan*, **21**(10):1936–1946, 1966.

[74] Y. B. Lyanda-Geller. *arXiv: 1107.3121.*

[75] R. V. Gorbachev, J. C. W. Song, G. L. Yu, A. V. Kretinin, F. Withers, Y. Cao, A. Mishchenko, I. V. Grigorieva, K. S. Novoselov, L. S. Levitov, and A. K. Geim. Detecting topological currents in graphene superlattices. *Science*, **346**(6208):448–451, 2014.

[76] W.-Y. Shan, J. Zhou, and D. Xiao. Optical generation and detection of pure valley current in monolayer transition-metal dichalcogenides. *Phys. Rev. B*, **91**:035402, Jan 2015.

[77] J. Karch, S. A. Tarasenko, E. L. Ivchenko, J. Kamann, P. Olbrich, M. Utz, Z. D. Kvon, and S. D. Ganichev. Photoexcitation of valley-orbit currents in (111)-oriented silicon metal-oxide-semiconductor field-effect transistors. *Phys. Rev. B*, **83**:121312, Mar 2011.

[78] L. E. Golub, S. A. Tarasenko, M. V. Entin, and L. I. Magarill. Valley separation in graphene by polarized light. *Phys. Rev. B*, **84**:195408, Nov 2011.

[79] R. R. Hartmann and M. E. Portnoi. *Optoelectronic properties of carbon-based nanostructures : steering electrons in graphene by electromagnetic fields.* (LAP Lambert Academic Publishing AG & Co KG), Saarbrucken, 2011.

[80] E. M. Lifshitz and L. P. Pitaevskii. *Statistical physics. Part 2.* Butterworth-Heinemann, Oxford, 1991.

[81] E. McCann and V. I. Fal'ko. Landau-level degeneracy and quantum hall effect in a graphite bilayer. *Phys. Rev. Lett.*, **96**:086805, Mar 2006.

[82] C. Jiang, V. A. Shalygin, V. Yu. Panevin, S. N. Danilov, M. M. Glazov, R. Yakimova, S. Lara-Avila, S. Kubatkin, and S. D. Ganichev. Helicity-dependent photocurrents in graphene layers excited by midinfrared radiation of a CO_2 laser. *Phys. Rev. B*, **84**:125429, Sep 2011.

[83] C. L. Kane and E. J. Mele. Z_2 topological order and the quantum spin hall effect. *Phys. Rev. Lett.*, **95**:146802, Sep 2005.

[84] H. Min, J. E. Hill, N. A. Sinitsyn, B. R. Sahu, Leonard Kleinman, and A. H. MacDonald. Intrinsic and rashba spin-orbit interactions in graphene sheets. *Phys. Rev. B*, **74**:165310, Oct 2006.

[85] Y. Yao, F. Ye, X.-L. Qi, S.-C. Zhang, and Z. Fang. Spin-orbit gap of graphene: First-principles calculations. *Phys. Rev. B*, **75**:041401, Jan 2007.

[86] M. Inglot, V. K. Dugaev, E. Ya. Sherman, and J. Barnaś. Enhanced photogalvanic effect in graphene due to rashba spin-orbit coupling. *Phys. Rev. B*, **91**:195428, May 2015.

[87] A. A Abrikosov and S. D. Beneslavskii. Possible existence of substances intermediate between metals and dielectrics. *Sov. Phys. JETP*, **32**:699, 1971.

[88] P. Hosur and X. Qi. Recent developments in transport phenomena in weyl semimetals. *Comptes Rendus Physique*, **14**(910):857 – 870, 2013.

[89] O. Vafek and A. Vishwanath. Dirac fermions in solids: From high-tc cuprates and graphene to topological insulators and weyl semimetals. *Annual Review of Condensed Matter Physics*, **5**(1):83–112, 2014.

[90] T. O. Wehling, A. M. Black-Schaffer, and A. V. Balatsky. Dirac materials. *Advances in Physics*, **63**(1):1–76, 2014.

[91] S. Murakami. Phase transition between the quantum spin hall and insulator phases in 3d: emergence of a topological gapless phase. *New Journal of Physics*, **9**(9):356, 2007.

[92] G. B. Halász and L. Balents. Time-reversal invariant realization of the weyl semimetal phase. *Phys. Rev. B*, **85**:035103, Jan 2012.

[93] S. M. Young, S. Zaheer, J. C. Y. Teo, C. L. Kane, E. J. Mele, and A. M. Rappe. Dirac semimetal in three dimensions. *Phys. Rev. Lett.*, **108**:140405, Apr 2012.

[94] S.-M. Huang, S.-Y. Xu, I. Belopolski, C.-C. Lee, G. Chang, B. Wang, N. Alidoust, G. Bian, M. Neupane, C. Zhang, S. Jia, A. Bansil, H. Lin, and M. Z. Hasan. A weyl fermion semimetal with surface fermi arcs in the transition metal monopnictide taas class. *Nature Communications*, **6**:7373 EP –, 06 2015.

[95] X. Wan, A. M. Turner, A. Vishwanath, and S. Y. Savrasov. Topological semimetal and fermi-arc surface states in the electronic structure of pyrochlore iridates. *Phys. Rev. B*, **83**:205101, May 2011.

[96] A. A. Burkov, M. D. Hook, and L. Balents. Topological nodal semimetals. *Phys. Rev. B*, **84**:235126, Dec 2011.

[97] V. Aji. Adler-bell-jackiw anomaly in weyl semimetals: Application to pyrochlore iridates. *Phys. Rev. B*, **85**:241101, Jun 2012.

[98] D. T. Son and B. Z. Spivak. Chiral anomaly and classical negative magnetoresistance of weyl metals. *Phys. Rev. B*, **88**:104412, Sep 2013.

[99] R. Okugawa and S. Murakami. Dispersion of fermi arcs in weyl semimetals and their evolutions to dirac cones. *Phys. Rev. B*, **89**:235315, Jun 2014.

[100] Y. Sun, S.-C. Wu, and B. Yan. Topological surface states and fermi arcs of the non-centrosymmetric weyl semimetals taas, tap, nbas, and nbp. *Phys. Rev. B*, **92**:115428, Sep 2015.

[101] F. D. M. Haldane. *arXiv: 1401.0529.*

[102] L. Lu, Z. Wang, D. Ye, L. Ran, L. Fu, J. D. Joannopoulos, and M. Soljačić. Experimental observation of weyl points. *Science*, **349**(6248):622–624, 2015.

[103] T. Liang J. W. Krizan W. Wang R. J. Cava J. Xiong, S. K. Kushwaha and N. P. Ong. *arXiv: 1503.08179.*

[104] B. Q. Lv, H. M. Weng, B. B. Fu, X. P. Wang, H. Miao, J. Ma, P. Richard, X. C. Huang, L. X. Zhao, G. F. Chen, Z. Fang, X. Dai, T. Qian, and H. Ding. Experimental discovery of weyl semimetal taas. *Phys. Rev. X*, **5**:031013, Jul 2015.

[105] C. Zhang, S.-Y. Xu, I. Belopolski, Z. Yuan, Z. Lin, B. Tong, N. Alidoust, C.-C. Lee, S.-M. Huang, H. Lin, M. Neupane, D. S. Sanchez, H. Zheng, G. Bian, J. Wang, C. Zhang, T. Neupert, M. Z. Hasan, and S. Jia. *arXiv: 1503.02630.*

[106] S.-Y. Xu, N. Alidoust, I. Belopolski, Z. Yuan, G. Bian, T.-R. Chang, H. Zheng, V. N. Strocov, D. S. Sanchez, G. Chang, C. Zhang, D. Mou, Yun Wu, L. Huang, C.-C. Lee, S.-M. Huang, B. K. Wang, A. Bansil, H.-T Jeng, T. Neupert, A. Kaminski, H. Lin, S. Jia, and M. Z. Hasan. Discovery of a weyl fermion state with fermi arcs in niobium arsenide. *Nat Phys*, **11**(9):748–754, 09 2015.

[107] B. Q. Lv, N. Xu, H. M. Weng, J. Z. Ma, P. Richard, X. C. Huang, L. X. Zhao, G. F. Chen, C. E. Matt, F. Bisti, V. N. Strocov, J. Mesot, Z. Fang, X. Dai, T. Qian, M. Shi, and H. Ding. Observation of weyl nodes in taas. *Nat Phys*, **11**(9):724–727, 09 2015.

[108] S.-Y. Xu, I. Belopolski, N. Alidoust, M. Neupane, G. Bian, C. Zhang, R. Sankar, G. Chang, Z. Yuan, C.-C. Lee, S.-M. Huang, H. Zheng, J. Ma, D. S. Sanchez, B. K. Wang, A. Bansil, F. Chou, P. P. Shibayev, H. Lin, S. Jia, and M. Z. Hasan. Discovery of a weyl fermion semimetal and topological fermi arcs. *Science*, **349**(6248):613–617, 2015.

[109] L. X. Yang, Z. K. Liu, Y. Sun, H. Peng, H. F. Yang, T. Zhang, B. Zhou, Y. Zhang, Y. F. Guo, M. Rahn, D. Prabhakaran, Z. Hussain, S. K. Mo, C. Felser, B. Yan, and Y. L. Chen. Weyl semimetal phase in the non-centrosymmetric compound taas. *Nat Phys*, **11**(9):728–732, 09 2015.

[110] H. B. Nielsen and M. Ninomiya. Absence of neutrinos on a lattice. *Nuclear Physics B*, **193**(1):173 – 194, 1981.

[111] H. B. Nielsen and M. Ninomiya. The adler-bell-jackiw anomaly and weyl fermions in a crystal. *Physics Letters B*, **130**(6):389 – 396, 1983.

[112] S. L. Adler. Axial-vector vertex in spinor electrodynamics. *Phys. Rev.*, **177**:2426–2438, Jan 1969.

[113] J. S. Bell and R. Jackiw. A pcac puzzle: $\pi 0\gamma\gamma$ in the σ-model. *Il Nuovo Cimento A (1965-1970)*, **60**(1):47–61, 1969.

[114] K. Nakada, M. Fujita, G. Dresselhaus, and M. S. Dresselhaus. Edge state in graphene ribbons: Nanometer size effect and edge shape dependence. *Phys. Rev. B*, **54**:17954–17961, Dec 1996.

[115] M. Fujita, K. Wakabayashi, K. Nakada, and K. Kusakabe. Peculiar localized state at zigzag graphite edge. *Journal of the Physical Society of Japan*, **65**(7):1920–1923, 1996.

[116] S. Ryu and Y. Hatsugai. Topological origin of zero-energy edge states in particle-hole symmetric systems. *Phys. Rev. Lett.*, **89**:077002, Jul 2002.

[117] A. R. Akhmerov and C. W. J. Beenakker. Boundary conditions for dirac fermions on a terminated honeycomb lattice. *Phys. Rev. B*, **77**:085423, Feb 2008.

[118] W. Chen, A. V. Andreev, and G. F. Bertsch. Conductance of a single-atom carbon chain with graphene leads. *Phys. Rev. B*, **80**:085410, Aug 2009.

[119] J. A. M. van Ostaay, A. R. Akhmerov, C. W. J. Beenakker, and M. Wimmer. Dirac boundary condition at the reconstructed zigzag edge of graphene. *Phys. Rev. B*, **84**:195434, Nov 2011.

[120] H. Bateman and A. Erdelyi. *Higher transcendental functions, Vol. 1.* (McGraw-Hill), New York, 1953.

[121] L. V. Keldysh. *Sov. Phys. JETP*, **6**:763, 1958.

[122] R. R. Haering and E. N. Adams. Esaki tunneling in the presence of magnetic fields. *Journal of Physics and Chemistry of Solids*, **19**(1):8 – 17, 1961.

[123] A. G. Aronov and G. E. Pikus. *Sov. Phys. JETP*, **24**:188, 1967.

[124] V. V. Cheianov and V. I. Fal'ko. Selective transmission of dirac electrons and ballistic magnetoresistance of $n\!-\!p$ junctions in graphene. *Phys. Rev. B*, **74**:041403, Jul 2006.

[125] A. V. Shytov, N. Gu, and L. S. Levitov. *arxiv: 0708.3081*.

[126] L. M. Zhang and M. M. Fogler. Nonlinear screening and ballistic transport in a graphene $p\!-\!n$ junction. *Phys. Rev. Lett.*, **100**:116804, Mar 2008.

[127] A. V. Andreev. Magnetoconductance of carbon nanotube $p - n$ junctions. *Phys. Rev. Lett.*, **99**:247204, Dec 2007.

[128] W. Chen, A. V. Andreev, E. G. Mishchenko, and L. I. Glazman. Decay of a plasmon into neutral modes in a carbon nanotube. *Phys. Rev. B*, **82**:115444, Sep 2010.

[129] J. Wang, X. Chen, B.-F. Zhu, and S.-C. Zhang. Topological *p*-*n* junction. *Phys. Rev. B*, **85**:235131, Jun 2012.

[130] Q. Li, D. E. Kharzeev, C. Zhang, Y. Huang, I. Pletikosic, A. V. Fedorov, R. D. Zhong, J. A. Schneeloch, G. D. Gu, and T. Valla. Chiral magnetic effect in zrte5. *Nat Phys*, **12**(6):550–554, 06 2016.

[131] S.-Y. Xu, N. Alidoust, I. Belopolski, Z. Yuan, G. Bian, T.-R. Chang, H. Zheng, V. N. Strocov, D. S. Sanchez, G. Chang, C. Zhang, D. Mou, Y. Wu, L. Huang, C.-C. Lee, S.-M. Huang, B. K. Wang, A. Bansil, H.-T. Jeng, T. Neupert, A. Kaminski, H. Lin, S. Jia, and M. Z. Hasan. Discovery of a weyl fermion state with fermi arcs in niobium arsenide. *Nat Phys*, **11**(9):748–754, 09 2015.

[132] J. Xiong, S. K. Kushwaha, T. Liang, J. W. Krizan, M. Hirschberger, W. Wang, R. J. Cava, and N. P. Ong. Evidence for the chiral anomaly in the dirac semimetal na3bi. *Science*, **350**(6259):413–416, 2015.

[133] A. A. Burkov and L. Balents. Weyl semimetal in a topological insulator multilayer. *Phys. Rev. Lett.*, **107**:127205, Sep 2011.

[134] C.-L. Zhang, S.-Y. Xu, I. Belopolski, Z. Yuan, Z. Lin, B. Tong, G. Bian, N. Alidoust, C.-C. Lee, S.-M. Huang, T.-R. Chang, G. Chang, C.-H. Hsu, H.-T. Jeng, M. Neupane, D. S. Sanchez, H. Zheng, J. Wang, H. Lin, C. Zhang, H.-Z. Lu, S.-Q. Shen, T. Neupert,

M. Z. Hasan, and S. Jia. Signatures of the adler–bell–jackiw chiral anomaly in a weyl fermion semimetal. *Nature Communications*, **7**:10735 EP –, 02 2016.

[135] Z. Wang Y. Zheng X. Yang, Y. Li and Z. Xu. *arxiv: 1506.03190.*

[136] C.-Z. Li, L.-X. Wang, H. Liu, J. Wang, Z.-M. Liao, and D.-P. Yu. Giant negative magnetoresistance induced by the chiral anomaly in individual cd3as2 nanowires. *Nature Communications*, **6**:10137 EP –, 12 2015.

[137] Y. Liu Z.-G. Chen S. Liang J. Cao X. Yuan L. Tang Q. Li T. Gu Y. Wu J. Zou C. Zhang, E. Zhang and F. Xiu. *arxiv: 1504.07698.*

[138] F. Arnold, C. Shekhar, S.-C. Wu, Y. Sun, R. D. dos Reis, N. Kumar, M. Naumann, M. O. Ajeesh, M. Schmidt, A. G. Grushin, J. H. Bardarson, M. Baenitz, D. Sokolov, H. Borrmann, M. Nicklas, C. Felser, E. Hassinger, and B. Yan. Negative magnetoresistance without well-defined chirality in the weyl semimetal tap. *Nature Communications*, **7**:11615 EP –, 05 2016.

[139] B. Z. Spivak and A. V. Andreev. Magnetotransport phenomena related to the chiral anomaly in weyl semimetals. *Phys. Rev. B*, **93**:085107, Feb 2016.

[140] H. Bateman and A. Erdelyi. *Higher transcendental functions, Vol. 2, Chap. 13.* (McGraw-Hill), New York, 1953.

[141] Yukihiro Okuno, Masashige Matsumoto, and Manfred Sigrist. Analysis of impurity-induced circular currents for the chiral superconductor Sr_2RuO_4. *Journal of the Physical Society of Japan*, **68**(9):3054–3061, 1999.

Appendix A

DERIVATION OF SKEW SCATTERING CROSS-SECTION OF QUASIPARTICLES IN A P+IP SUPERCONDUCTORS

Here we obtain the scattering probability $W_{\mathbf{pp}'}$ in Eq. (2.8) in Chapter 2 that gives rise to anomalous transport properties. For simplicity we consider point-like impurities whose scattering matrix elements are independent of momentum, $V_{\mathbf{pp}'} = V_0$. Skew scattering appears beyond the lowest Born approximation as a result of a particular structure of the order parameter in $p_x + ip_y$ superconductors. We note that even weak impurities, $|\nu V_0| \ll 1$, lead to the existence of bound states in $p_x + ip_y$ superconductors with binding energies $E_b \sim |\Delta||\nu V_0|^2$. [141] Therefore low energy quasiparticles undergo resonant scattering. We show below that this also results in energy-dependent skew scattering.

The scattering properties of a single impurity are described by the T-matrix. In a superconductor, for each initial and final momenta $\mathbf{p}'$ and $\mathbf{p}$ the T-matrix acquires an additional 2×2 structure in the Nambu-Gorkov space. We denote these 2×2 matrices by $\hat{T}_{\mathbf{pp}'}$. The quasiparticle scattering amplitude is given by the on-shell matrix element $\hat{T}_{\mathbf{pp}'} \equiv \langle \mathbf{p}|\hat{T}|\mathbf{p}'\rangle$, with $|\mathbf{p}\rangle$ being the two component quasiparticle wave function. Using the Fermi Golden rule the scattering probability can be expressed as

$$W_{\mathbf{pp}'} = 2\pi n_i V |\hat{T}_{\mathbf{pp}'}|^2 \tag{A.1}$$

where V is the system volume and n_i is the impurity concentration. The T-matrix obeys the Lipmann-Schwinger equation

$$\hat{T}_{\mathbf{pp}'} = \hat{V}_{\mathbf{pp}'} + \sum_{\mathbf{p}''} \hat{V}_{\mathbf{pp}''} \hat{G}_0(\mathbf{p}'') \hat{T}_{\mathbf{p}''\mathbf{p}'}, \tag{A.2}$$

For point-like impurities, $\hat{V}_{\mathbf{pp}'} = V_0 \hat{\tau}_3$ (with $\hat{\tau}_i$ being the Pauli matrices in the Nambu-Gorkov space), the T-matrix depends only on the energy E. Thus Eq. (A.2) simplifies to

$$\hat{T}(E) = V_0\hat{\tau}_3 + V_0\hat{\tau}_3 \sum_{\mathbf{p}} \hat{G}_0(\mathbf{p})\hat{T}(E) \tag{A.3}$$

The order parameter of $p_x + ip_y$ superconductor can be expressed as $\Delta(p_x + ip_y)/p_F = \Delta\exp(i\varphi_{\mathbf{p}})$ where the phase $\varphi_{\mathbf{p}}$ is momentum-dependent such that $\cos\varphi_{\mathbf{p}} = p_x/p_F$ and $\sin\varphi_{\mathbf{p}} = p_y/p_F$. This leads to the BCS Hamiltonian

$$\hat{H}(\mathbf{p}) = \begin{pmatrix} \xi_{\mathbf{p}} & \Delta e^{i\varphi_{\mathbf{p}}} \\ \Delta e^{-i\varphi_{\mathbf{p}}} & -\xi_{\mathbf{p}} \end{pmatrix}, \tag{A.4}$$

and hence the Green function $\hat{G}_0(\mathbf{p}) \equiv \left(E - \hat{H}(\mathbf{p})\right)^{-1}$,

$$\hat{G}_0(\mathbf{p}) \;=\; \frac{1}{E^2 - \epsilon_{\mathbf{p}}^2} \begin{pmatrix} E + \xi_{\mathbf{p}} & \Delta e^{i\varphi_{\mathbf{p}}} \\ \Delta e^{-i\varphi_{\mathbf{p}}} & E - \xi_{\mathbf{p}} \end{pmatrix}. \tag{A.5}$$

Replacing the summation over $\mathbf{p}$ with $V\int d^3p/(2\pi\hbar)^3 \approx \nu V \int d\xi_{\mathbf{p}} \int d\varphi_{\mathbf{p}}/2\pi$, where V is the volume of the sample and ν is the density of state at Fermi surface, and using Eq. (A.3) and Eq. (A.5), we obtain for the T-matrix,

$$\hat{T}(E) = \begin{pmatrix} \frac{V_0}{1+\pi\nu V_0 E/\sqrt{\Delta^2-E^2}} & 0 \\ 0 & \frac{-V_0}{1-\pi\nu V_0 E/\sqrt{\Delta^2-E^2}} \end{pmatrix}$$

The pole of the T-matrix describes the subgap bound state [141] with the binding energy $E_b = \Delta/\sqrt{1+(\pi\nu V_0)^2}$. For the energy in the continuum, $|E| > \Delta$, we obtain the T-matrix in the form

$$\hat{T}(E) = \begin{pmatrix} f(E)e^{i\delta_E} & 0 \\ 0 & -f(E)e^{-i\delta_E} \end{pmatrix} \tag{A.6}$$

where δ_E is given by Eq. (9) in the main text, and

$$f(E) = \frac{V_0}{\sqrt{1 + (\pi\nu V_0)^2 E^2/(E^2 - \Delta^2)}}. \tag{A.7}$$

The quasiparticle scattering amplitude is given by the on-shell matrix elements between two quasiparticle states with energy $\epsilon = \sqrt{\Delta^2 + \xi_{\mathbf{p}}^2} = \sqrt{\Delta^2 + \xi_{\mathbf{p}'}^2}$,

$$\hat{T}_{\mathbf{p}\mathbf{p}'} = \langle \mathbf{p}|\hat{T}(\epsilon)|\mathbf{p}'\rangle. \tag{A.8}$$

In a $p_x + ip_y$ superconductor the Bogoliubov amplitudes carry a momentum-dependent phase $\varphi_{\mathbf{p}}$,

$$\langle \mathbf{p}| = \frac{e^{-i\mathbf{p}\cdot\mathbf{r}}}{\sqrt{V}}(u_{\mathbf{p}} e^{-i\varphi_{\mathbf{p}}}, v_{\mathbf{p}}), \tag{A.9}$$

where $u_{\mathbf{p}}$ and $v_{\mathbf{p}}$ have the standard BCS form and are independent of the momentum direction,

$$u_{\mathbf{p}} = \sqrt{\left(1 + \xi_{\mathbf{p}}/\epsilon_{\mathbf{p}}\right)/2}, \quad v_{\mathbf{p}} = \sqrt{\left(1 - \xi_{\mathbf{p}}/\epsilon_{\mathbf{p}}\right)/2} \tag{A.10}$$

Substituting Eqs. (A.9) and (A.10) into (A.8) we get

$$\begin{aligned} \left|\hat{T}_{\mathbf{pp}'}\right|^2 &= \frac{f^2(\epsilon)}{V}\Big\{ \left(u_{\mathbf{p}} u_{\mathbf{p}'} - v_{\mathbf{p}} v_{\mathbf{p}'}\right)^2 + 2 u_{\mathbf{p}} u_{\mathbf{p}'} v_{\mathbf{p}} v_{\mathbf{p}'} \\ &\quad \times \left[1 - \cos(2\delta_\epsilon + \varphi_{\mathbf{p}} - \varphi_{\mathbf{p}'})\right] \Big\} && \text{(A.11)} \\ &= \frac{1}{2}\frac{f^2(\epsilon)}{V}\left(1 + \frac{\xi_{\mathbf{p}}\xi_{\mathbf{p}'} - \Delta^2}{\epsilon_{\mathbf{p}}^2}\right) + \\ &\quad \frac{f^2(\epsilon)}{V}\frac{\Delta^2}{2\epsilon_{\mathbf{p}}^2}\left[1 - \cos\left(2\delta_\epsilon + \varphi_{\mathbf{p}} - \varphi_{\mathbf{p}'}\right)\right] && \text{(A.12)} \end{aligned}$$

Substituting this result into Eq. (A.1), and recalling that for weak impurities, $|\pi\nu V_0| \ll 1$, the scattering rate in the normal state is $\tau^{-1} = 2\pi n_i \nu V_0^2$ we obtain the scattering probability in the form of Eqs. (2.8) and (2.10) in Chapter 2.

Appendix B

DERIVATION OF MAGNETOCONDUCTANCE OF A WEYL P-N JUNCTION IN A TILTED MAGNETIC FIELD

Here we derive the expression for the conductance of the p-n junction in a tilted magnetic field, Eq. (5.9) in Chapter 5. Let the magnetic field be in the x-z plane at an angle θ with the z-axis, $\mathbf{B} = B(\sin\theta, 0, \cos\theta)$. Near the crossing point, $U(z) \approx -eEz$, the Dirac Hamiltonian reads

$$H \;=\; v\,\boldsymbol{\sigma}\cdot\left(-i\hbar\boldsymbol{\nabla} - \frac{e}{c}\mathbf{A}\right) - eEz,$$

We work in the Landau gauge $\mathbf{A} = B(0, x\cos\theta - z\sin\theta, 0)$, and consider motion of an electron with a conserved wavenumber k_y along the y-axis. Let us make a unitary transformation which amounts to rotation about the x-axis in pseudospin space;

$$\sigma_x \to \sigma_x, \quad \sigma_y \to \sigma_z, \quad \sigma_z \to -\sigma_y. \tag{B.1}$$

Upon this transformation the Hamiltonian becomes

$$\frac{H}{\hbar v} \;=\; \begin{pmatrix} k_y - \frac{x\cos\theta - z\sin\theta}{l_B^2} - \frac{z}{l_E^2} & -i\partial_x + \partial_z \\ -i\partial_x - \partial_z & -k_y + \frac{x\cos\theta - z\sin\theta}{l_B^2} - \frac{z}{l_E^2} \end{pmatrix}.$$

Let us now rescale the variables. We will measure coordinates in units of the magnetic length l_B, and energy in units of $\hbar v/l_B$. The rescaled Dirac equation on spinor $\psi_{\mathbf{k}} = (u_{\mathbf{k}}, v_{\mathbf{k}})^T$ becomes

$$(i\partial_x + \partial_z)u_{\mathbf{k}} \;=\; \left[x\cos\theta - k_y - z\left(\sin\theta + \frac{cE}{vB}\right)\right]v_{\mathbf{k}}, \tag{B.2a}$$

$$(i\partial_x - \partial_z)v_{\mathbf{k}} \;=\; \left[k_y - x\cos\theta + z\left(\sin\theta - \frac{cE}{vB}\right)\right]u_{\mathbf{k}}. \tag{B.2b}$$

We now apply the operator $i\partial_x - \partial_z$ to (B.2a) and combine the result with (B.2b) multiplied by $-k_y + x\cos\theta - z\left(\sin\theta + \frac{cE}{vB}\right)$. Similarly, we apply $i\partial_x + \partial_z$ to (B.2b) and combine the result with (B.2a) multiplied by $k_y - x\cos\theta + z\left(\sin\theta - \frac{cE}{vB}\right)$. This yields the system of second order partial differential equations,

$$\hat{h}\begin{pmatrix} u_{\mathbf{k}} \\ v_{\mathbf{k}} \end{pmatrix} = \left[\sin\theta\sigma_x - \left(\cos\theta - i\frac{cE}{vB}\right)\sigma_y\right]\begin{pmatrix} u_{\mathbf{k}} \\ v_{\mathbf{k}} \end{pmatrix}, \tag{B.3}$$

where $\hat{h}$ is given by

$$\hat{h} = \left(\partial_x^2 + \partial_z^2\right) - \left[(k_y - x\cos\theta + z\sin\theta)^2 - z^2\left(\frac{cE}{vB}\right)^2\right]. \tag{B.4}$$

Diagonalizing the matrix in the right hand side of Eq. (B.3) and denoting its eigenvalues by

$$\beta_\pm = \pm i\sqrt{\left(\frac{cE}{vB}\right)^2 - 1 + 2i\cos\theta\,\frac{cE}{vB}}, \tag{B.5}$$

we get two Schrödinger equations for the appropriate linear combinations of $u_{\mathbf{k}}$ and $v_{\mathbf{k}}$,

$$\hat{h}\,\varphi_\pm = \beta_\pm\varphi_\pm.$$

Changing the coordinates from x, z to ξ, ζ via

$$\begin{pmatrix} x - \frac{k_y}{\cos\theta} \\ z \end{pmatrix} = \begin{pmatrix} \cos\alpha & \sin\alpha \\ -\sin\alpha & \cos\alpha \end{pmatrix}\begin{pmatrix} \xi \\ \zeta \end{pmatrix}, \tag{B.6}$$

where the rotation angle α is given by

$$\tan 2\alpha = \frac{\sin 2\theta}{\cos 2\theta + \left(\frac{cE}{vB}\right)^2}, \tag{B.7}$$

we can write the Schrödinger operator $\hat{h}$ in the form

$$\hat{h} = \partial_\xi^2 - |\lambda_-|\xi^2 + \partial_\zeta^2 + \lambda_+\zeta^2,$$

where

$$\lambda_\pm = \frac{1}{2}\left[\left(\frac{cE}{vB}\right)^2 - 1 \pm \sqrt{\left[\left(\frac{cE}{vB}\right)^2 - 1\right]^2 + 4\cos^2\theta\left(\frac{cE}{vB}\right)^2}\right]. \tag{B.8}$$

Rescaling the coordinates ξ and ζ to $\tilde{\xi} = |\lambda_-|^{1/4}\xi$ and $\tilde{\zeta} = \lambda_+^{1/4}\zeta$ we we reduce the Shrödinger operator $\hat{h}$ to the simple form $\hat{h} = \sqrt{|\lambda_-|}\left(\partial^2_{\tilde{\xi}} - \tilde{\xi}^2\right) + \sqrt{\lambda_+}\left(\partial^2_{\tilde{\zeta}} + \tilde{\zeta}^2\right)$.

The solutions corresponding to the scattering problem may be written in the form $\varphi(\tilde{\xi},\tilde{\zeta}) = f(\tilde{\xi})g(\tilde{\zeta})$, where $f(\tilde{\xi})$ has the form $f(\tilde{\xi}) = e^{-\tilde{\xi}^2/2}H_n(\tilde{\xi}), \quad n = 0, 1, 2\cdots$. Here n is the Landau level index and $H_n(x)$ is the Hermite polynomial. The function $g(\tilde{\zeta})$ satisfies the Weber equation

$$\frac{d^2g}{d\tilde{\zeta}^2} + \left[\tilde{\zeta}^2 - (i + q_n^2)\right] g(\tilde{\zeta}) = 0, \tag{B.9}$$

with

$$q_n^2 = 2n\sqrt{\frac{|\lambda_-|}{\lambda_+}} - \frac{\beta_\pm \mp \sqrt{|\lambda_-|}}{\sqrt{\lambda_+}} - i.$$

Eq. (B.9) describes scattering of a nonrelativistic particle at an inverted parabolic potential. The corresponding transmission amplitude is given by $\exp(-\pi q_n^2/2)$. Using the fact that $\mathrm{Re}\beta_\pm = \pm\sqrt{\lambda_-}$ we get the transmission coefficient in the form

$$\mathcal{T}_n = \exp\left(-2\pi n\sqrt{\frac{|\lambda_-|}{\lambda_+}}\right). \tag{B.10}$$

Accounting for the Landau Level degeneracy and the number of Weyl nodes, we get the junction conductance in the form of Eq. (5.9) in Chapter 5,

$$G = \frac{e^2}{h}\sum_i \frac{S\cos\theta}{2\pi l_B^2}\,\frac{\cos\alpha_i}{1 - e^{-2\pi\sqrt{|\lambda_{i-}|/\lambda_{i+}}}}, \tag{B.11}$$

$$\tan 2\alpha_i = \frac{\sin 2\theta}{\cos 2\theta + (cE_i/vB)^2}. \tag{B.12}$$

Here i labels the quantities pertaining to the crossing point for the i-th Weyl node. The presence of $\cos\alpha$ accounts for the fact that Klein tunneling occurs along ζ-axis which makes the angle α with the z-axis by α. For a magnetic field normal to the junction ($\theta = 0$) this equation reproduces Eq. (5.8) in Chapter 5.

VITA

Songci Li was born in Sichuan, China. He obtained his Bachelor's degree in University of Science and Technology of China in 2012. He then went to University of Washington, Seattle in 2012 for a PhD degree and finished this dissertation in June, 2017.